

Contents

1	Current monitoring	
	<i>Real-time particle identification</i>	3
1.1	Motivation	4
1.2	Requirements	4
1.3	Device specifications	5
1.4	Pulse parameters	5
1.5	Applications	7
1.6	Description of the firmware	7
	1.6.1 Design constraints	8
	1.6.2 Analysis module	9
	1.6.3 Area and width measurement	11
1.7	Control and data interface	14
	1.7.1 Software	14
	1.7.2 Data readout	14
1.8	Performance results	15
	1.8.1 Tests with a pulse generator	15
	1.8.2 Comparison between the charge-sensitive and current spectroscopy .	18
1.9	Source calibration	18
	1.9.1 Pulse classification	18
	1.9.2 Data acquisition	25
	1.9.3 Scatter plots	27
1.10	Applications in neutron instrumentation	37
	1.10.1 Thermal neutron flux monitoring	37
	1.10.2 Fusion power monitoring	41
	1.10.3 Recoil proton monitoring	45
	1.10.4 Fast and thermal neutron monitoring	46
1.11	Conclusion	49
	Bibliography	51

Chapter 1

Current monitoring

Real-time particle identification

Diamond sensors have a very fast signal response due to their low capacitance. The electrical signal created by drifting charge carriers retains its shape without significant distortion. When the sensor is used together with a fast current amplifier with a high broadband limit (~ 2 GHz) and a readout device with a similar limit, the information about the drifting charges is retained. For instance, a proton creates the free e-h pairs along its trajectory. The electrons and holes start drifting immediately. Those closest to the electrodes recombine quickly whereas those at the opposite side contribute to the induced signal for longer. The resulting signal is therefore a triangular pulse with a steep rising edge and a gentle falling edge. It is possible to determine the drift velocity of the charge carriers by measuring the width of the pulse, as was done in chapter ???. Furthermore, it is possible to determine with a certain probability what is the type of incident radiation, judging by the shape of the induced pulse. This, however, only applies to sCVD diamond material. Its uniform carbon lattice allows the ionisation profiles to retain their shape, unlike in pCVD material, laden with grain boundaries, or in even in silicon where the shape is deformed due to p-n junction non-uniformities.

This chapter describes an application that carries out particle identification by means of the pulse shape analysis. It was developed for measuring activity of a neutron reactor. In this case the device has to be able to filter out the photon background with a rate several orders of magnitude higher than the neutron rate. Overall detected rate in a neutron reactor can easily exceed 10^8 particles $\text{cm}^{-2}\text{s}^{-1}$, depending on the distance of the detector from the reactor core. The device has to be able to cope with such high rates. It also needs to be dead time free or at least close to that, to minimise the counting error. At these rates, it still has to be able to identify the types of pulse. This type of online analysis cannot be done in software. It has to be implemented in an FPGA.

1.1 Motivation

Pulse shape analysis (PSA) is a common software tool for analysing sensor response to incident particles. It is usually done by means of software that runs over big amounts of data that have been acquired and saved to storage. This offline analysis can be repeated and improved. However, the saved data take up a lot of storage space. In addition, saving raw waveform data requires a system capable of a high data throughput and fast data storing. For instance, an oscilloscope can save up to 100 signal waveforms per second. This means that there is a high measurement dead time. To avoid the high dead times, the software algorithms can be ported to the FPGA where they analyse the incoming signal in real time. The signal is then discarded and only the analysis results are saved, decreasing the storage space significantly.

The offline pulse shape analysis has already been used for particle identification with a diamond sensor [1, 2]. An effort has been made to implement an online and real time application for this analysis by porting the algorithms into an FPGA. This section first describes the device specifications. Then it describes in detail the PSA algorithms and the structure of the code. Afterwards it discusses the performance results, which showcase the limitations of the device. Finally it describes the data acquired with radioactive sources and in neutron reactors.

1.2 Requirements

Chapter ?? shows that the shape is heavily dependent on several factors, such as environmental temperature and received irradiation dose. At temperatures lower than 150 K the signal from an α starts deteriorating due to recombination of charges in the charge cloud. Sensor irradiation, on the other hand, introduces charge traps, which cause the signal to decay exponentially. These two factors are a significant limitation for particle identification. Priming can improve the charge collection and longterm stability of the pulse shapes. To improve the measurement further, a high bias voltage has to be applied, increasing the measurement SNR.

Factor	Operating range
Sensor material	sCVD diamond
Sensor thickness	500 μm
Temperature	150 K – 400 K
Radiation dose	1×10^{13} neq $\text{cm}^{-2} \text{s}^{-1}$
Charge carriers	holes
Bias voltage	$\sim 1 \text{ V } \mu\text{m}^{-1}$
Signal-to-noise	5

Table 1.1: Limitations to particle identification.

1.3 Device specifications

The ROSY box has a single BNC input with the termination $50\ \Omega$ or $1\ M\Omega$ with a DC or AC coupling. The analog chain has a 250 MHz bandwidth limit. The input range can be set from $\pm 50\ \text{mV}$ up to $\pm 5\ \text{V}$. The signal offset can be set to any value within this range. The ADC samples this signal with an 8-bit precision at a rate of up to 5 GSPS. The PSA uses the highest sampling to achieve width measurement resolution of 0.2 ns. The spectroscopic application does not need such a fine timing resolution and therefore operates at a reduced sampling rate of 0.8 ns. The amplitude resolution depends on the chosen input range, but at 256 ADC counts per sample, it can be as low as $0.39\ \text{mV s}^{-1}$ at the range of $\pm 50\ \text{mV}$ and as high as $39\ \text{mV s}^{-1}$ at the range of $\pm 5\ \text{V}$.

The logic structure of the PSA is designed using VHDL and runs on Xilinx Virtex 5. The PSA is capable of a maximum counting rate of 1.56×10^8 pulses per second, yielding a 6.4 ns double pulse resolution. The analysis is more time consuming; the maximum throughput rate of the pulse shape analysis is $\sim 6 \times 10^6$ pulses per second. This means that after every pulse, the device has a dead time of approximately (200 ± 15) ns, depending on the width of the pulse being analysed. Any pulse arriving during the analysis of the previous one is counted, but not analysed. Any two pulses with the distance between the rising edges lower than 6.4 ns are counted as a single pulse.

The device is very sensitive to noise pick-up. Therefore the setup must be designed to minimise the pick-up by means of proper shielding, use of high-quality cables etc. The relatively low bandwidth limit filters out some high-frequency noise, but not the ringing or higher noise spikes. That is the task for the PSA.

1.4 Pulse parameters

A signal pulse on the input is parametrised during the analysis process. The PSA measures its amplitude, area, width at the baseline and at half the maximum amplitude, and the slope of its falling edge, as shown in figure 1.1. The amplitude is the difference between the baseline and the highest sample in the pulse and is given in ADC counts as an 8-bit value. The area is defined as the sum of amplitudes of all samples between two defined boundaries within the pulse. The width is defined as the number of samples with a value higher than a set amplitude threshold. If the threshold is at half the maximum amplitude, the resulting width is *full width at half maximum* (FWHM). The falling slope is the maximum negative difference between values of two samples and is given in ADC counts per sample.

The most important pulse parameter is the pulse area. It is equal to the deposited charge of the particle. It is also directly proportional to the energy of the particle that is stopped in the sensor. The area distribution of a particle is therefore its energy spectrum. This is the target measurement for all radiation types. All subsequent parameters are shown as a function of the pulse area:

- FWHM [w, a]

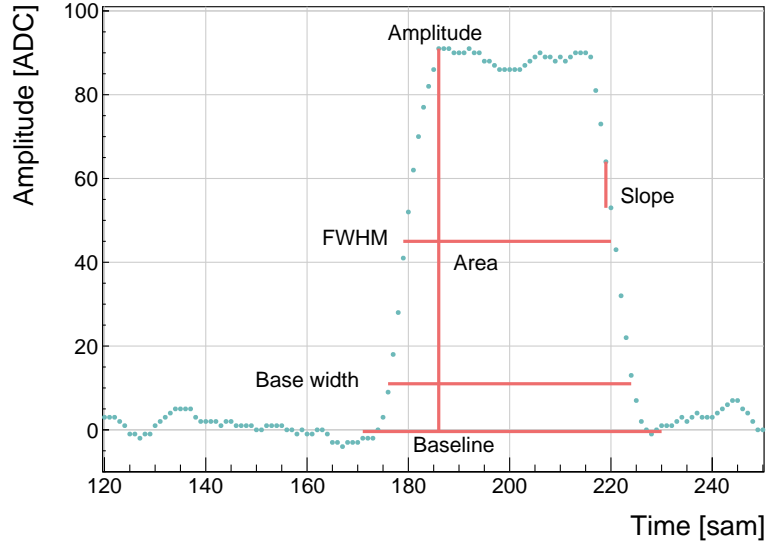


Figure 1.1: Pulse parametrisation.

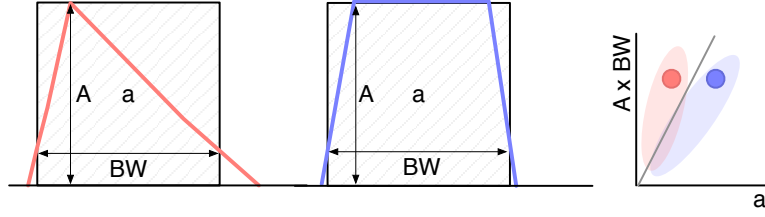


Figure 1.2: Form Factor. The red and blue dot in the right plot are the value entries of the two pulses shown. The red and blue oval shapes depict the regions for the values expected for triangular and rectangular pulses. By carefully choosing the linear qualifier (black line) and taking only the entries below the cut rectangular pulses can be identified.

- Base width [bw, a]
- Amplitude [A, a]
- Amplitude \times Base width [$A \times bw$, a]
- Base width-FWHM [bw-w, a]
- Falling slope [s, a]

The Amplitude \times Base width qualifier is referred to as the *calculated area*. The ratio between the calculated area (a) and the measured area ($A \times BW$) is the *Form Factor* and is shown in figure 1.2. A Form Factor value of 1 means that the pulse shape is similar to a rectangle. A value of 2 means that the pulse has a triangular shape.

1.5 Applications

The FPGA firmware is designed for systems instrumented with CIVIDEC amplifiers and CIVIDEC sCVD diamond detectors. Three applications are available: *Spectroscopy*, *Pulse Shape Analysis* and *Counter*, each optimised for a specific task. Their capabilities are described below. The firmware runs in ROSY, a readout system produced by CIVIDEC.

Spectroscopy is a tool for measuring energy spectra of radioactive sources. It is used in combination with the CIVIDEC Cx spectroscopic charge amplifier. The signal from the charge amplifier is analysed in real time. The FPGA measures the maximum amplitude of the signal. The amplitude value is ready at the end of the pulse and is stored in the amplitude histogram. Immediately after, the analysis is reset and the system is ready for a new acquisition. Upon request from the software, the histogram is read out, during which the analysis is paused. In addition to the histogram building, the firmware can also store raw pulse waveforms, which can be then read out by the software. The maximum allowed throughput is 1 million counts per second.

Pulse Shape Analysis is a tool for measuring energy spectra of radioactive sources, with an additional feature. It can identify the type of radiation detected by the diamond detector. By means of the pulse analysis it can subtract the background radiation and only measure the signals from the defined radiation source. It is used in combination with the CIVIDEC C2 broadband current amplifier. The firmware receives a current pulse from the detector and digitises it. The pulse is then analysed and parametrised. The analysis module measures its maximum amplitude, full width at half maximum (FWHM), baseline amplitude, falling slope and its area. Then it compares the obtained pulse parameters with the qualifiers set by the software and determines what type of radiation hit the diamond detector. Depending on the qualifiers, the pulse can either be *accepted* or *rejected*. The firmware then stores the parameters of the analysed pulse into histograms. Two histograms exist for each parameter: one for all pulses and one for accepted pulses. In addition, there is one 2D histogram (a scatter plot), which can plot two parameters one with respect to the other. Upon request from the software, all histograms are read out, during which the analysis is paused. The maximum allowed throughput is 1 million counts per second.

Counter is a tool that measures the count rate and the mean time during counts. It is used in combination with the CIVIDEC Cx, C6 or C2 amplifier. It contains one histogram which holds the information about the mean time during counts. The counter is operational also during the readout of the histogram. The highest counting rate with enabled histogram writing is $3 \times 10^7 \text{ s}^{-1}$.

1.6 Description of the firmware

The applications are built on top of the Picotech platform. The base code handles the communication between the software and the hardware. Furthermore, it provides the interface

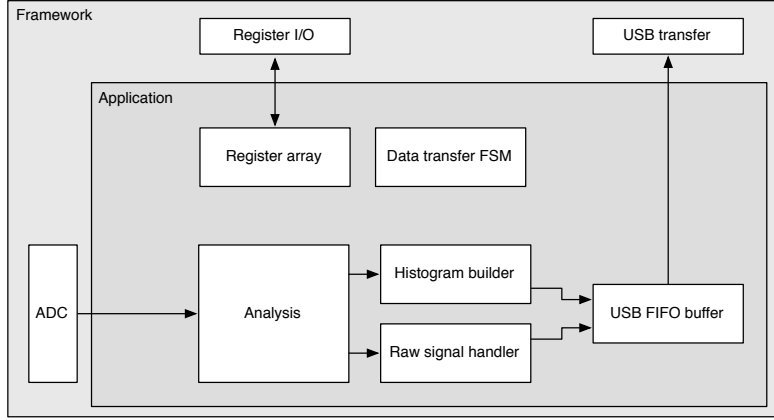


Figure 1.3: Firmware design structure.

to the ADC data, the input/output registers and the USB data transfer. The applications have a set of modules that handle the data input and output and a module for signal analysis, as shown in figure 1.3. The data handling modules are very similar in all the applications to ensure compatibility of the communication between software and firmware and the readout data format. The analysis module, however, is different from one application to the other. The data handling layer is the same for all applications and consists of the final state machine (FSM), the histogram builder, the raw signal handler, the USB FIFO buffer and the register array.

The firmware is written entirely in VHDL. The diagram in figure 1.3 shows the module architecture. The ADC provides the module with 32 digitised signal samples every clock cycle (6.4 ns). The signal is routed directly to the pulse analyser and into the raw signal handler. The analyser outputs are connected to the I/O registers and to histogram buffers. Both the histogram buffers and raw signal buffers are connected to the USB FIFO through a multiplexor. The firmware communication to the controller is done via input/output (I/O) registers (control and status registers, counters) and serially via USB (histogram data, waveforms).

1.6.1 Design constraints

Speed The ADC provides 32 8-bit samples on every 6.4 ns clock cycle. It is not possible to e.g. sum all 32 values in a single cycle, because the summation takes too long to complete. This is why the summation has to be pipelined and carried out in three cycles. This adds up to the analysis duration, which in turn decreases the maximum pulse rate.

Firmware size The PSA application makes use of a number of FIFO and RAM buffers to store the pulse waveforms and histograms. 48 32k block RAM modules have been used for the implementation, maxing out the available block RAM memory space on this FPGA. The analysis algorithm also takes up a significant portion of the FPGA. Many of the operations are carried out on 256-bit long numbers received from the ADC, which quickly fills up the

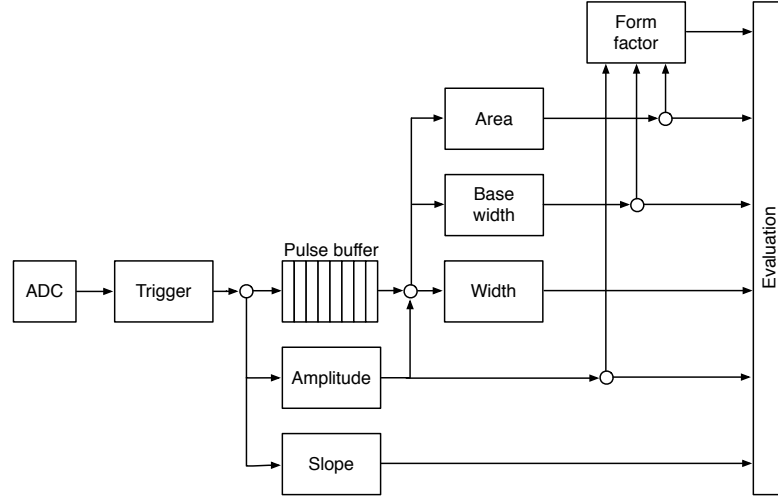


Figure 1.4: Code design plan.

available logic. This is also why the place and route procedure takes a long time.

Power consumption The reduction of the power consumption is not crucial for the intended applications.

1.6.2 Analysis module

This module is different for different applications. The Pulse Shape Analysis (PSA) application has the most complex module design. The spectroscopy application only uses a small part of that design and the Counter application an even smaller one.

The analysis (or parametrisation) is carried out in several steps, as shown in figure 1.4. The triggering block starts the readout upon signal threshold crossing. The maximum slope of the falling edge is observed. The Amplitude block calculates the pulse height and retains the maximum amplitude while pushing the signal into the pulse buffer. Then the entire pulse is clocked out of the buffer while its FWHM, baseline width and area are measured. Finally, the Form factor is calculated. At the end the Evaluation block takes in all the parametrised information and classifies the pulse according to user-defined cuts.

Triggering module handles signal polarity swapping, triggering on threshold and defining the trigger window. The real-time processing algorithm allows for a positive or an inverted input signal. However, the PSA only handles positive-polarity pulses. Therefore a negative signal is swapped in the *triggering* block. Signal analysis and readout are then triggered when the signal crosses a user-defined threshold. In addition, the signal has to be over the threshold for a defined number of samples. This is to avoid triggering on noise spikes. A double clock cycle delay is used on the signal to make sure that the recorded signal window includes the rising edge of the pulse as well as some baseline before it. A *trigger active* signal marks a window that contains the entire pulse including some baseline signal before

and after it. The trigger can be vetoed by three signals: if the pulse analysis is still taking place, if the input signal exceeds the maximum voltage range or if the data transfer FSM is pausing the analysis due to data transfer to the controller.

Amplitude block calculates the pulse height from the difference between the pulse and the baseline. It also finds the position of the maximum amplitude within the clock cycle. It receives 32 8-bit samples from the triggering block every clock cycle. Time delays in the logic prevent it to find the maximum value of the 32 samples within one clock cycle (6.4 ns). Therefore the decision logic has been pipelined in three stages, which means that the final maximum value is ready three clock cycles after the end of the pulse.

Pulse buffer is a FIFO that stores the signal while its amplitude is being measured. At the end of the pulse the FIFO is read out so that the remaining measurements can take place.

Width block uses the maximum amplitude to determine the *half-maximum* and to measure the FWHM. To do so, it counts the samples that are above the half-maximum amplitude. However, this method might also count high enough noise spikes before or after the pulse. Hence an improved method, which “cleans” the measurement of unintentional additional noise, has been implemented. It is described in section 1.6.3.

Baseline width block is the same as the Width block, but it measures the width either at 50 %, 25 %, 12.5 % or 6.25 %, depending on the setting in the register. It also makes use of the special method described in 1.6.3 to avoid overestimations due to including noise in the measurement.

Area block measures the pulse area by summing up the amplitude values of the samples in the pulse. The boundaries of the summation are defined with the crossing of the amplitude above a certain threshold. Only the samples between those boundaries are summed up. The boundaries can be set at 50 %, 25 %, 12.5 % or 6.25 % of the maximum amplitude of the pulse. The area measurement makes use of the same routine as the FWHM and Baseline width block to remove the potential outlying samples.

Falling slope block measures the highest negative difference between amplitudes of two adjacent samples, thus getting the maximum negative slope of the pulse. It is an experimental routine, only used for academic purposes.

Form factor block is used as a special qualifier for particle identification. It compares the weighted measured area of the pulse with its weighted calculated “form”, which is defined as the multiplication of the measured amplitude and baseline width. The equation is as follows:

$$x \cdot a - y \cdot A \cdot BW \geq 0, \quad (1.1)$$

where a is the measured area, A is the amplitude, BW is the baseline width and x and y the weighting factors for the measured and calculated area, respectively. The output of the block is the boolean result of this equation.

Evaluation block takes in all the parameters from the analysis blocks and compares them against the user-defined qualifiers. If the parameters are within the bounds, the pulse is accepted, otherwise it is rejected. The corresponding counters within the block are incremented.

1.6.3 Area and width measurement

The routine for measuring pulse area and width must have a specific algorithm implemented to carry out the measurements correctly. The core point is that the routine precisely defines the edges of a pulse. It does so by means of *vector cleaning*, presented in figure 1.5. An important input, beside the ADC data and the measurement threshold, is the position of the sample with the highest amplitude.

The signal arrives from the ADC as a set of 32 8-bit samples every clock cycle with a period of 6.4 ns. All 32 samples are compared against the width measurement threshold. If a sample value is equal or higher than this threshold, a binary 1 is set in a 32-bit *vector* on the position corresponding to the position of the sample in the incoming ADC data set. The resulting vector might also include some noise at the edges of the pulse, depending on the height of the width measurement threshold. The old routine simply counts the binary ones in this vector to get the pulse width. This works well for measuring the FWHM because the threshold was high. However, for width measurements at 25 %, 12.5 % or 6.25 % of the pulse height this might already become a problem, because the noise might be counted in as well. This is why the new routine cleans the outliers in this vector before counting the remaining ones in the clean vector.

The routine starts from the position of the maximum height. It follows the vector in both ways and finds the first falling edge (0 at this position and 1 at the previous one). From there on it rewrites any binary 1 with a binary 0. The resulting clean vector only has one bunched set of binary ones which are summed, yielding a precise pulse width. The area measurement is similar - it only integrates over the samples marked in the clean vector. Both measurement routines, for area and for width, are implemented separately so that the area routine can have a different threshold set.

This section explains how the algorithm is designed. First, the idea for it was tested using Excel and was only afterwards ported to the VHDL. The underlying algorithm first cleans the vector. Then it passes the cleaned vector either to the width or area measurement, as shown in figures 1.6 and 1.7. The width measurement module only sums the ones in the vector whereas the area measurement module sums the data samples marked by the cleaned vector. Both modules issue a *valid* signal when they finish the measurement.

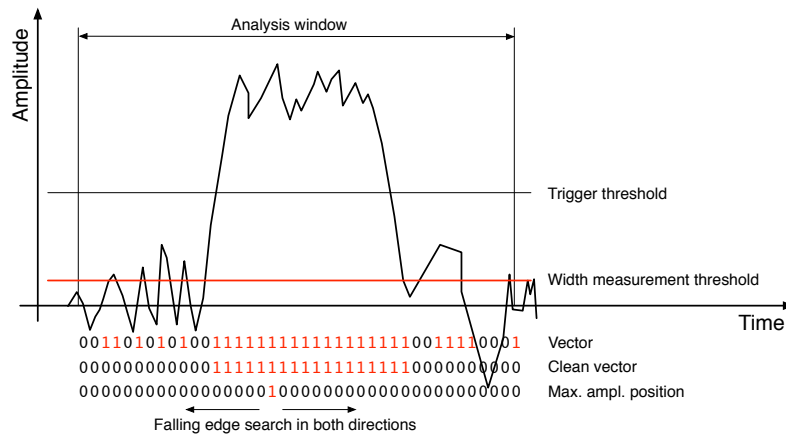


Figure 1.5: A sample pulse. The first vector shows which samples are above the width measurement height. The second vector is a clean vector. The third line shows the position of the maximum amplitude. The vector cleaning algorithm starts from the maximum amplitude and continues in both ways along the vector.

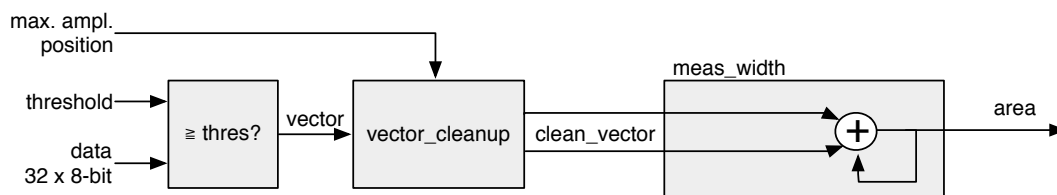


Figure 1.6: This block counts the remaining binary ones in the clean vectors and outputs this value as the pulse width.

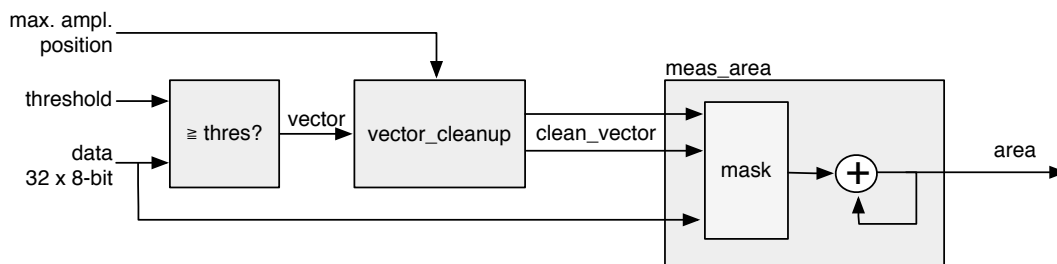


Figure 1.7: This block masks the input data with the clean vector and sums the remaining samples.

Vector cleaning

This is the most important block. Its inputs are: *vector*, *parsing active*, *position of the max. amplitude (PA)* and *its delay (DA)*. PA is a 32-bit binary number that shows the position of the sample with the maximum amplitude within the data block whereas the DA tells us how many clock cycles after the start of the parsing this PA block is. The vector cleaning module is designed as a final state machine (FSM) with the states IDLE,

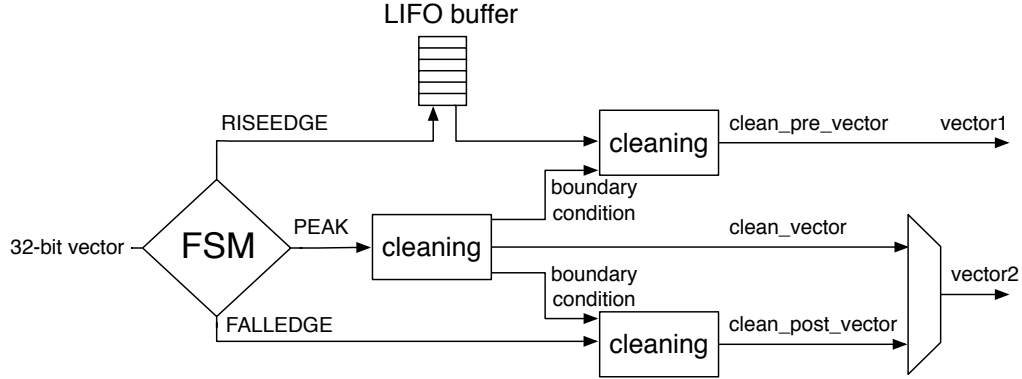


Figure 1.8: Vector cleaning routine outputs two vectors - one forward in time and one back in time from the peak of the pulse.

RISEEDGE, PEAK, FALLEDGE and READY. The FSM is idle until it receives the *active* signal from the external module, marking that the vector parsing has commenced. It switches to RISEEDGE, which starts two procedures: 1) it fills the vector of the pulse's rising edge into a last-in-first-out (LIFO) buffer and 2) counts down from the DA value. When this counter reaches 0, the FSM changes its state to PEAK because the current vector on the input is the one containing the maximum amplitude. This data block is sent through the *peak algorithm*, which cleans the vector. The FSM switches to FALLEDGE state. Now both the previously buffered vector of the rising edge and current vector of the falling edge go through the *pre- and post- algorithm* where they are cleaned, but they get their boundary conditions from the *peak algorithm*. The output of this module is therefore two cleaned vectors in parallel – one forward in time and the other backwards.

Algorithm

The underlying algorithm is sequential - it carries out a logic operation on vector bit on position 0, uses the output of this operation for the operation on bit on position 1 and so on. This means that it has to carry out 32 logic operations per clock cycle. With each operation taking approximately 0.3 ns, the entire logic chain takes approximately 10 ns to complete. With only 6.4 ns per clock cycle, this means timing errors would occur. To fix the problem, a more complicated *decimated algorithm* has been designed. It consists of two parallel logic chains. Each of the two only takes every second bit into account (Chain one: 0, 2, 4 ..., 30. Chain two: 1, 3, 5 ..., 31). This makes the chains effectively 16 bits long. The algorithm is run on the two chains and the results are merged together at the end as shown in figure 1.10. This effectively reduces the number of sequential logic operations to 18, which is within the timing constraints.

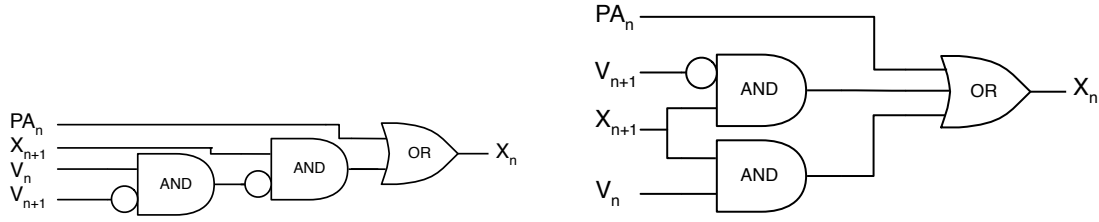


Figure 1.9: One logic step in the algorithm chain before and after Karnaugh minimisation.

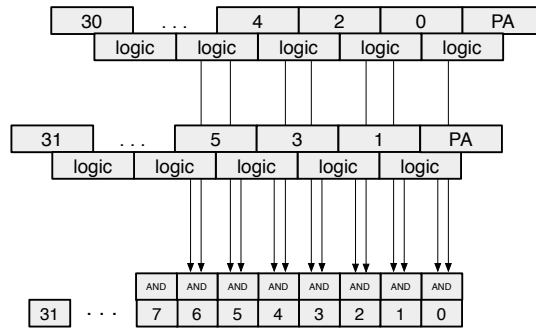


Figure 1.10: The vector is divided into two 16-bit logic chains. The algorithm logic is then run on the two chains separately. The results are then merged into one 32-bit clean vector by using a set of AND gates.

1.7 Control and data interface

Communication between the device and the controller PC is done via the API functions provided by the producer. In addition, the API used by CIVIDEC has access to several extra functions. These allow the user to download a customised bitfile to the FPGA, access the I/O registers and use the USB data transfer.

1.7.1 Software

The software has been designed in C++ in several levels of abstraction. Figure 1.11 shows the structure of the classes. The classes Device, PSA and RawSignalHandler are there to make it easier to read and understand the controller code. In principle the PSfunctions can also be accessed directly by the controller, but for this the instruction sequences must be well known and understood.

1.7.2 Data readout

The device records the data in two forms - as signal waveforms and as histograms of analysed pulse parameters. Both are available upon request from the controller. Only one of the two can be transferred via the USB line at a time.

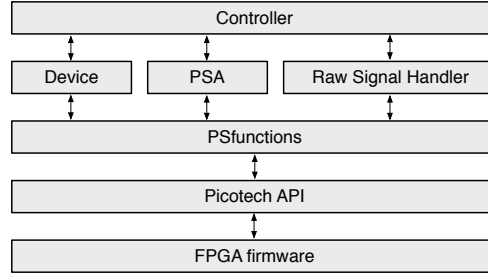


Figure 1.11: Abstraction levels of the controller software.

The waveforms are saved into a FIFO buffer, which can hold up to 64 pulses of the length of ~ 500 samples. The data format for each pulse is such that it starts with a header containing the pulse timestamp and the sequential number, continues with the data samples and ends with a header containing all the measured parameters (width, amplitude, area, falling slope and form factor). When the FIFO is full, it issues a flag, which tells the controller that the data buffer is ready for readout.

The histograms are implemented into the FPGA's Block RAM. Their sizes range from 256 to 4'096 bins (8-bit to 12-bit histograms, respectively), depending on the required histogram resolution. For instance, the width parameter is measured with a 0.2 ns resolution and the expected maximum pulse width is less than 20 ns. This yields the maximum range of 100 bins, making an 8-bit histogram sufficiently large. The amplitude histogram range is defined by the 8-bit resolution of the ADC. The area measurement, however, yields higher values and can therefore have a more refined 12-bit binning. Finally, a single 12-bit 2D histogram is included, with six bits for every axis. It is used as an online scatter plot for comparing two measured parameters. An example for it is a comparison of the width against the area, which can help the user determine the cuts that need to be applied to the measurement. All implemented 2-D plots are shown in section 1.9.

1.8 Performance results

The PSA was tested in the laboratory first using a pulse generator and then with a radioactive sources. This section contains the results of the performance tests.

1.8.1 Tests with a pulse generator

Trigger rate

A pulse generator was used to verify the highest achievable rate at which the PSA still analyses every incoming pulse. The final state machine implemented in the pulse analysis module prevents the triggering block from issuing a trigger due to an incoming pulse if the previous analysis is still in ongoing. Given that all the pulses were of the same length, the analysis duration was always the same. When the time between the incoming pulses was

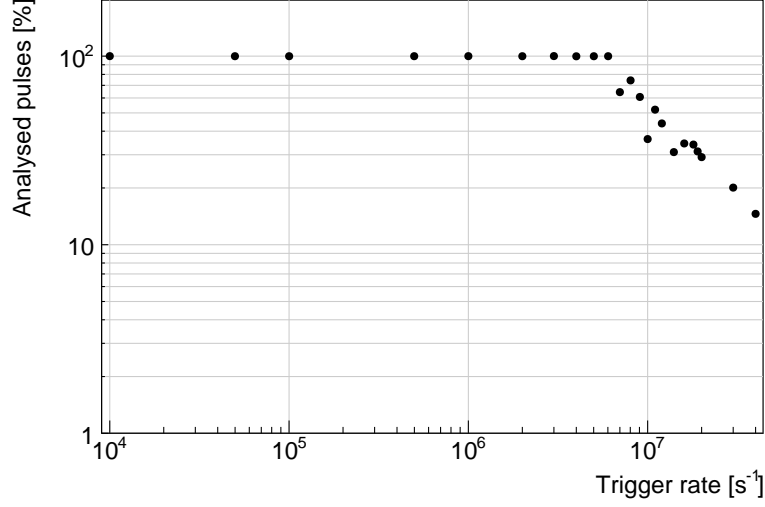


Figure 1.12: This figure shows the capability of the device to analyse all arriving pulses for a range of input frequencies. The highest achievable rate with zero lost pulses is $6 \times 10^6 \text{ s}^{-1}$.

shorter than the time of the analysis, the pulses were not analysed. Figure 1.12 shows the sharp decline in the percentage of the analysed pulses when reaching the rate of 6 MHz. Therefore the overall analysis duration for a 10 ns pulse is approximately 200 ns.

Linearity

A pulse generator was used to verify the linearity of the measurements across all input ranges. The pulse width and the amplitude were varied and measured both with the oscilloscope and the PSA to estimate the systematic error of the PSA measurements with respect to those taken by the oscilloscope. The results are shown in figures 1.13a and 1.13b. The measured amplitude error e_{ampl} is within $\pm 3 \%$ of the real value throughout the amplitude range. The width error e_{width} , however, increases significantly in the lower width range. This stems from the low bandwidth limit of the PSA, which affects the pulse shape via a slow rising and falling time, effectively smearing the pulse along the time axis. Therefore the PSA cannot measure rectangular pulses shorter than 2 ns.

Stability

The input pulse signal was superimposed with the white noise generated by a CIVIDEC noise generator with a variable attenuation. The mixed signal yielded pulses with an SNR ranging from 5 (very noisy) to 100 (noise negligible). The PSA then performed the pulse parametrisation at different SNRs without changing the pulse shape. The results of the measurement errors for amplitude, width and area are shown in figures 1.14a, 1.14b and 1.14c. The amplitude is highly overestimated at a low SNR (high noise). This is because the algorithm takes the peak of the signal as the maximum amplitude and these peaks are higher with a higher noise. Therefore the e_{ampl} is always positive and increasing with

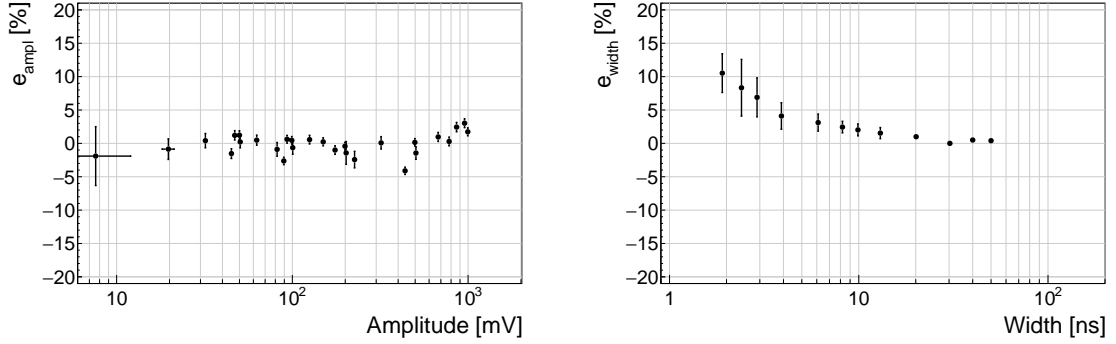


Figure 1.13: These figures show the measurement errors for amplitude (left) and width (right) across the measurement range.

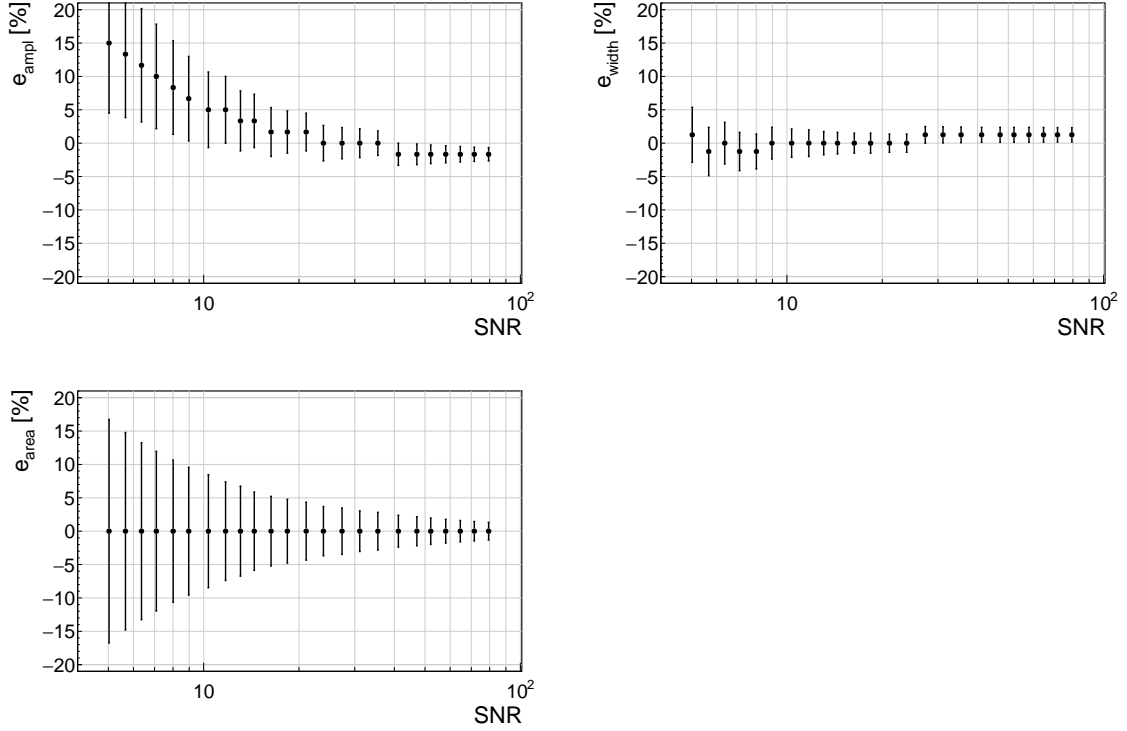


Figure 1.14: These figures show the measurements errors for amplitude (top left), width (top right) and area (bottom left) as a function of the signal-to-noise ratio.

increasing noise. The width measurement, on the other hand, is stable even for the low SNR. The e_{width} does not exceed $\pm 5\%$. Finally, the mean of the area measurement error e_{area} is always 0, but the spread of the error increases with noise. This means that the increased noise only affects the resolution of the measured area spectrum, not its position.

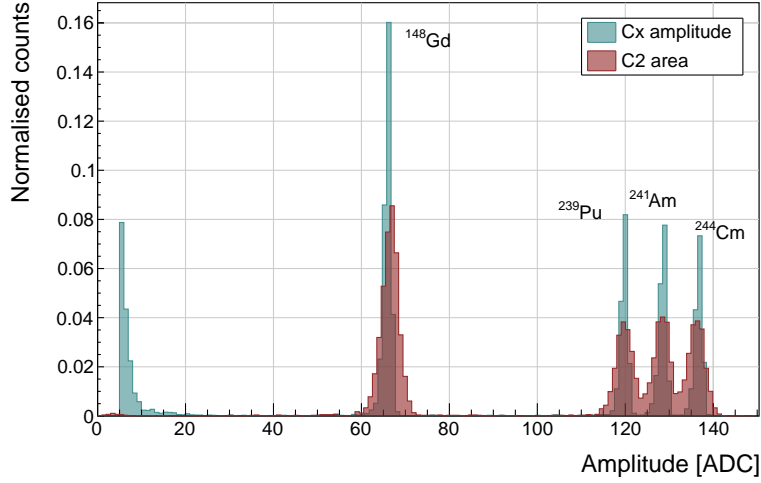


Figure 1.15: Energy spectrum of a quadruple- α source using a CIVIDEC Cx spectroscopic amplifier and a CIVIDEC C2 current amplifier.

Conclusion

The results show that: 1) the amplitude, area and width measurement are linear for pulses at least 2 ns wide, 2) the highest rate of the PSA algorithm is $\sim 6 \times 10^6$ pulses per second and 3) the lowest SNR where the algorithm still functions is ~ 5 , but the area measurement spread at that SNR is significant.

1.8.2 Comparison between the charge-sensitive and current spectroscopy

The calibration was done using a quadruple- α source containing ^{148}Gd , ^{239}Pu , ^{241}Am and ^{244}Cm . Each of the radioactive elements emits α particles with a specific energy: 3.2 MeV, 5.2 MeV, 5.5 MeV and 5.8 MeV. The PSA in combination with the CIVIDEC C2 current amplifier was compared against the 8-bit spectroscopic application in combination with the CIVIDEC Cx spectroscopy amplifier.

Figure 1.15 shows the energy spectrum acquired by the two amplifiers. The ^{241}Am peak measured by the CIVIDEC Cx amplifier has an RMS of 0.8 ADC, which corresponds to a 32 keV energy resolution. For comparison, the CIVIDEC C2 broadband current amplifier measures this peak with an RMS of 1.9 ADC, which corresponds to a 75 keV energy resolution. Therefore the energy spectrum measured by the current amplifier has a factor of 2.3 lower energy resolution.

1.9 Source calibration

1.9.1 Pulse classification

Pulses induced by a specific radiation type have a specific pulse shape and therefore similar parameters. This section outlines the parameter space for several types of radiation. Ta-

ble 1.2 lists the types of radiation and their respective pulse shapes. The types have been sorted into classes for easier discussion. The table includes the radioactive sources that emit these particles.

Class	Particle type	Current signal	Source
A	α	Square pulse, h^- drift	^{241}Am
B	α	Square pulse, e^- drift	^{241}Am
C	β	Triangular pulse	^{90}Sr
D	γ	Triangular pulse	^{60}Co
E	n	Mixed pulse shapes	^{239}Pu
F	p	Mixed pulse shapes	^{239}Pu

Table 1.2: Current pulse classification.

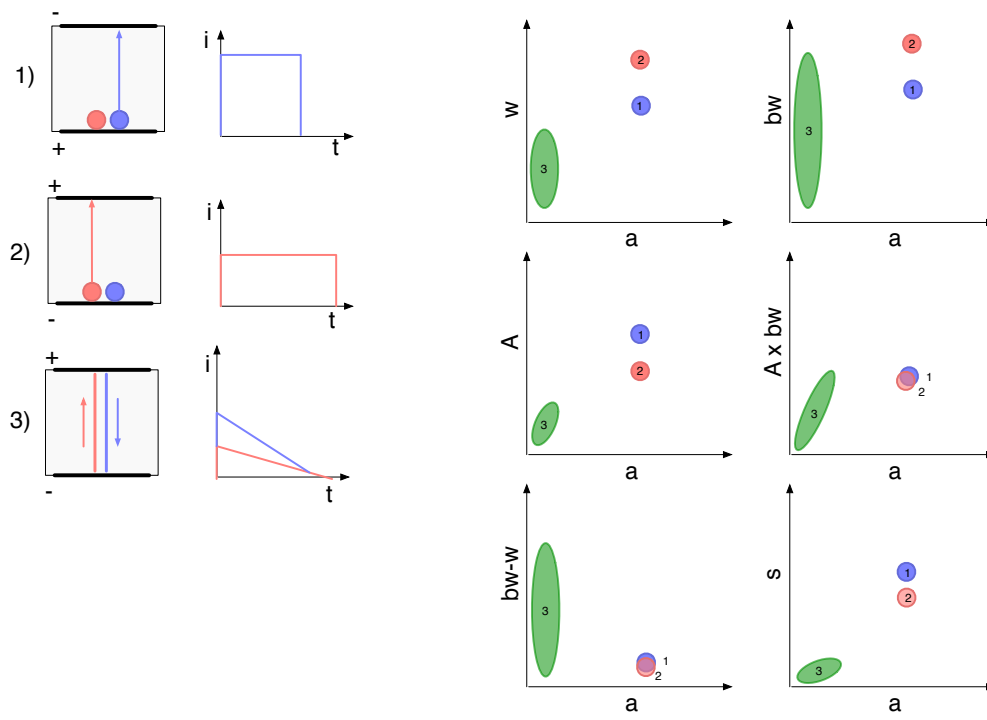


Figure 1.16: Class A, B, C, D.

Class A, B, C, D

An α particle deposits all its energy at the point of entry in the sensor. Depending on the polarity of the sensor bias voltage, either holes or electrons drift through the sensor, inducing a rectangular current pulse.

Schematic 1) in figure 1.16 shows the positive charge carriers drifting through the sensor and the current pulse they induce – Class A. Holes produce a short and high rectangular pulse. The parametric “fingerprint” of these current pulses is shown on the right side of figure 1.16, marked with number 1. All α particles deposit the same amount of charge. The width and the base width are always the same as the drift velocity of the charge carriers does not change regardless of the number of carriers drifting. The base value is slightly higher due to the rise and fall time of the current signal. The amplitude is the same for all pulses. The same goes for the calculated area (a product of the amplitude and base value). For an ideal pulse, the coefficient between the measured area and the calculated area for a rectangular pulse is 1. The difference between the base width and the width is close to 0 and depends on the rise and fall time of the current signal defined by the electronics. The falling slope of the signal depends on the amplitude of the signal, therefore it is constant for a nominal pulse.

Schematic 2) in figure 1.16 shows the negative charge carriers drifting through the sensor and the current pulse they induce – Class B. Electrons produce a wide and low rectangular pulse. Parametrically Class B differs from Class A in the width, base width, amplitude and slope. The former two are higher due to lower drift velocity of electrons. The amplitude is proportionally higher to preserve the constant pulse area due to a constant deposited charge.

Schematic 3) in figure 1.16 shows the configuration of the deposited charge created by an incident β particle – Class C. The positive and negative charge carriers induce a triangular pulse while drifting to their respective electrodes. The number of electrons and holes created differs from pulse to pulse, but follows a Landau distribution, as discussed in previous chapters. The amplitude of the pulse is linearly dependent on the initial number of created carriers, but has a higher coefficient than that of Class A or B. The same goes for the width and base width. The width of the pulses is lower than that of Class A and B. The base width, however, can already be close to Class A and B for the widest Class C pulses. The coefficient between the measured and calculated area is close to 2. The difference between the base width and width is a wide distribution. The falling slope is a low value for triangular pulses of all amplitudes.

γ particles interact with the diamond via Compton scattering, exciting an electron, which in turn ionises the sensor. Therefore the predicted pulse shape – Class D – will be similar to that of β particles – Class C.

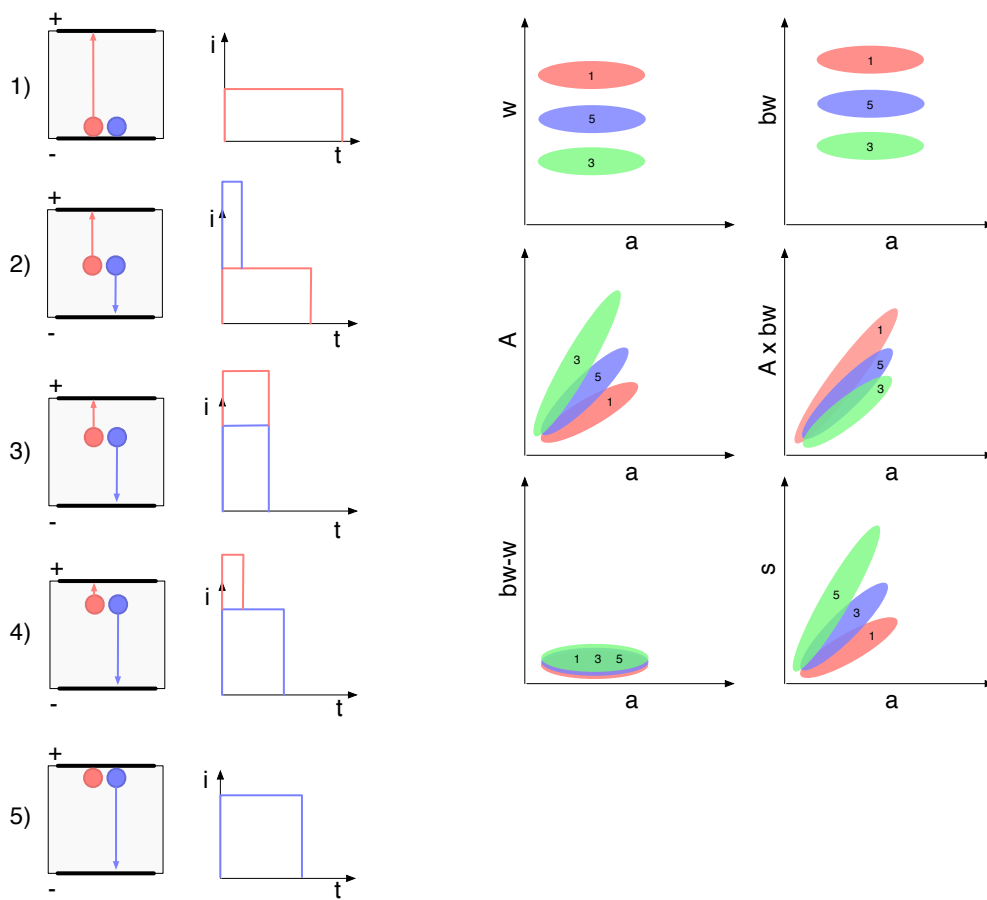


Figure 1.17: Class E.

Class E

Neutrons interact with the core of the carbon atoms, producing a range of particles ranging from γ , β and α to protons. Neutrons are therefore a source of Class A, B, C, D, E and F pulses. Class E is a special case whereby α particles are created at various points throughout the sensor. These particles immediately deposit all their energy and the created electrons and holes that drift to their respective electrodes induce a pulse with of a specific shape. Schematics in figure 1.17 show examples of an α creation in the sensor at five depths.

Schematics 1) and 5) are equal to Class B and A type. The difference here is that the created α particles have a range of energies and therefore the deposited charge has a wide range. Their parametric fingerprint is similar to that of Class A and B, but is now spread over a wide range. The width and base width are equal across the measured range, the same holds for the difference between base width and width. The amplitude for both 1 and 5 increases linearly with the area.

Schematic 2) shows a carrier creation in the middle of the sensor and its respective current pulse. The holes drift faster and reach their respective electrode before the electrons reach the opposite side. The resulting pulse has a high peak at the start where both charges contribute to the signal and a long rectangular tail pertaining to the electron drift. Schematic 4) is similar to 2), with a difference that in this case the electrons contribute to the initial peak. These two cases are not shown in the parameter space.

Schematic 3) shows a special case in which the created electrons and holes reach their respective electrodes at the same time. This results in a short and high rectangular shaped current pulse. It is narrower from 1) and 5). Its amplitude increase as a function of the area is faster than for the other two. The same goes for the slope. Inversely, the calculated area increase as a function of the area is slower due to a smaller base width.

In summary, Class E pulses stem from neutron interactions at the electrodes or in the bulk, forming three distinct lines.

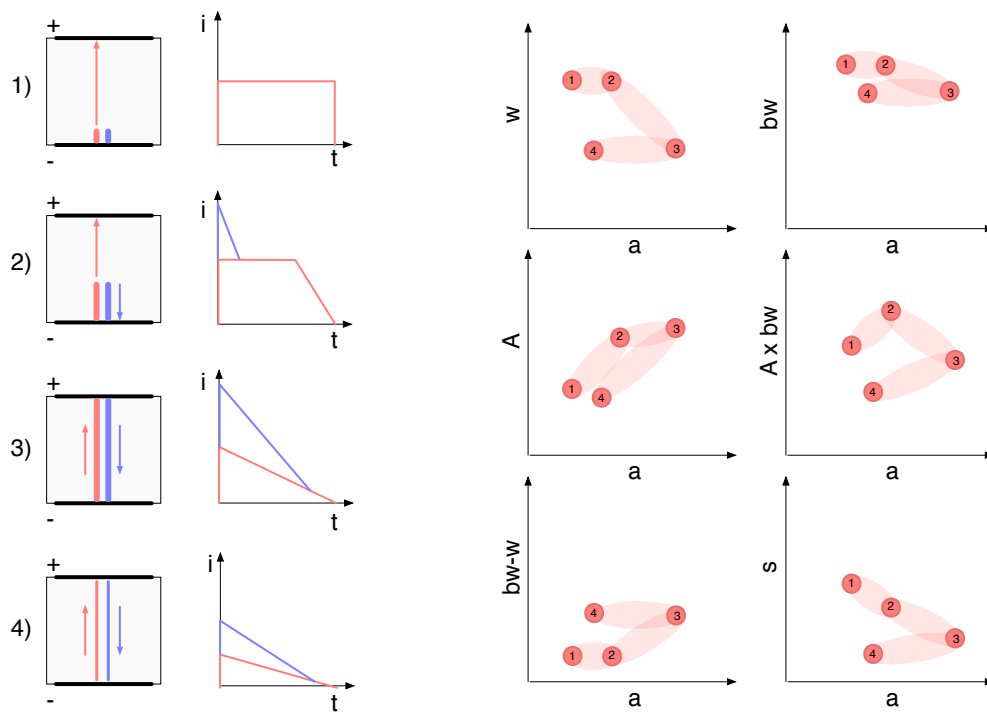


Figure 1.18: Class F.

Class F

Protons can produce a range of pulse shapes, depending on their energy. High-energy MIPs fly through the sensor and produce a triangular pulse equal to that of β . Those with a low energy get stopped in the sensor, inducing a pulse with a complex shape. Class F comprises protons created by a neutron interaction with a carbon atom, referred to as recoil protons. For reasons of clarity the examples shown below stem from a neutron interaction at the negatively charged electrode. In addition, the direction of the recoil proton is always in the direction of the opposite electrode.

Schematic 1) shows a creation of a low-energy recoil proton. It deposits all its energy within a few μm , inducing a Class B rectangular pulse. It also resembles the Class B in the parameter space.

Schematic 2) shows a proton that travels for a third of the sensor width before being stopped. The trace it leaves induces a pulse with an initial peak due to the contribution of the drifting holes and a gentle falling edge at the end. Its width and base width are still close to the nominal value. The amplitude is significantly higher due to the initial peak. As a consequence, the calculated area is higher as well. The difference between the base width and width is still nominal. The slope value decreases due to a less pronounced falling edge of the pulse.

Schematic 3) shows a corner case whereby the recoil proton that is stopped at the opposite electrode. It induces a high triangular pulse. Its width is significantly lower due to the high amplitude. The base width, however, remains almost the same. Therefore the difference between the base width and width increases. The slope continues decreasing.

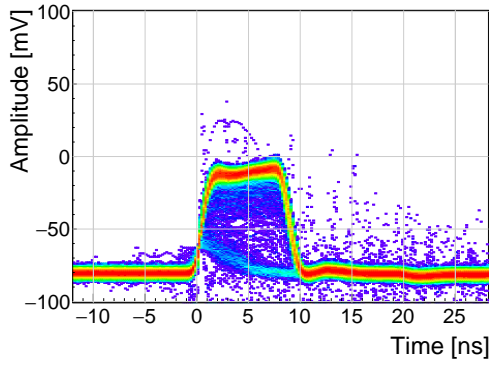
Schematic 4) shows a high-energy recoil proton that exits the sensor with a high velocity. According to the Bethe-Bloch such a highly energetic particle deposits less charge than that with a low energy. The resulting current pulse therefore has a lower amplitude while preserving the width. Its slope is also lower due to the lower amplitude.

1.9.2 Data acquisition

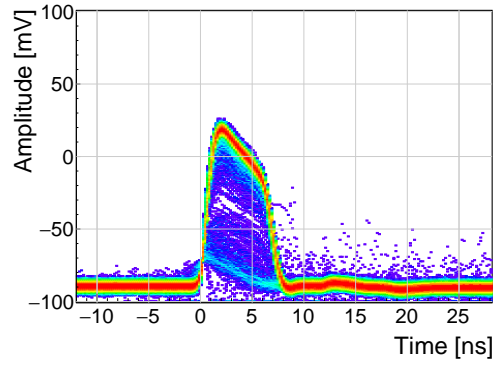
The operation of the pulse shape analysis has been tested using several radioactive sources. In particular, an α , a β and a γ source have been used. Each source has been placed on top of the diamond detector and left for a predefined time depending on its activity. Table ?? shows the sources used, the time of exposure and their rate during data acquisition. The data for the α source have been taken for both polarities.

Run	Source	Radiation	Energy [MeV]	Time [h]	Triggers	Rate [s^{-1}]	Bias [V]
1	^{241}Am	α	5.5	17	10558	0.17	500
2	^{241}Am	α	5.5	18	11454	0.18	-500
3	^{90}Sr	β	2.3	0.42	1.07e6	1'000	500
4	^{60}Co	γ	1.3	0.28	1.34e6	3'300	500
5	^{239}Pu Be	n	1–10	2.5	1.5e6	230	500

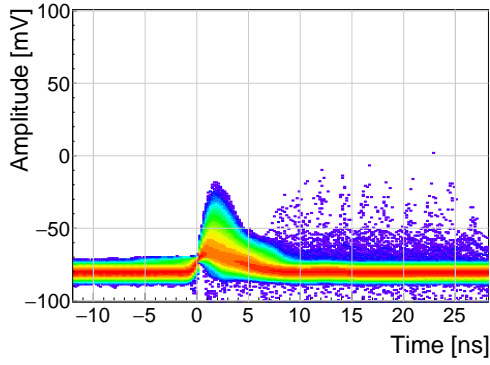
Table 1.3: Measurements carried out at Atominstitut.



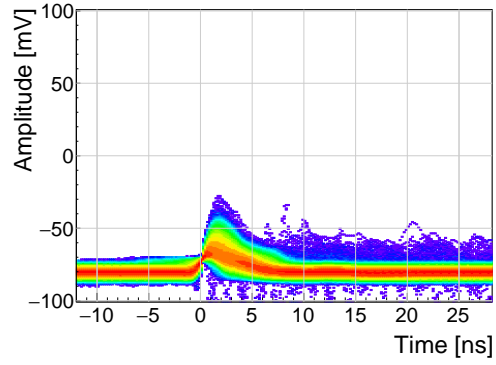
(a) ^{241}Am , e^- collection.



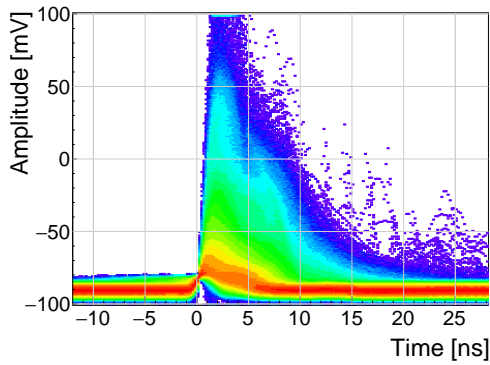
(b) ^{241}Am , h^+ collection.



(c) ^{90}Sr .



(d) ^{60}Co .



(e) ^{239}Pu Be.

Figure 1.19: Accumulated current pulses for all runs.

Figure 1.19a shows a set of current pulses induced by the α particles whereby only the electrons drift through the sensor. The great majority of particles creates a defined number of charge carriers. According to the FWHM of the pulse, the electrons drift for 9 ns before reaching the opposite electrode. The pulse amplitude is stable during the drift, with a gentle positive inclination. This hint on a weak negative space-charge built up across the sensor. Some pulses have a lower amplitude while retaining the width; the smaller pulse area means that there are fewer drifting charge carriers than a nominal value. This shows that some incident α already lose a part of their energy while traveling through the air before hitting the sensor. Furthermore, there is a number of low-amplitude triangular pulses which are created by incident γ particles. Finally, the scarce entries above the baseline after the pulse stem from interference pulses.

Figure 1.19b also shows the α -induced current signals, but for the hole collection. The number of holes created is equal to the number of created electrons, therefore the collected charge is the same for both. This means that the area of the current pulse is equal to that in figure 1.19a. The pulses are only 6 ns wide, which confirms that hole mobility in diamond is $\sim 30\%$ higher than that of electrons at room temperature. Therefore the current pulse must be higher to preserve the area. The pulses have a steep negative droop. This is due to a strong negative space-charge built up during preceding measurements with a neutron source. Furthermore, some pulses induced by a lower energy α have a lower amplitude and hence a lower pulse area. Finally, the γ -created triangular pulses are still present.

Figure 1.19c shows the triangular pulses created by the incident β particles. Most have a low amplitude that is close to the trigger threshold (red coloured line). Those below the threshold are not visible by the PSA. The entries behind the pulses are either interference pulses or β pulses following the first pulse.

Figure 1.19d shows the triangular pulses created by the incident γ particles. The distribution is very similar to that created by the incident electrons in figure 1.19c. This is expected – γ particles interact with the sensor via Compton scattering, freeing an electron which in turn ionises the sensor. Therefore the resulting current pulses of an incident γ are similar to those of an incident β .

Figure 1.19e shows that the neutron source causes the widest variety of pulse shapes - triangular and rectangular as well as those in between. This stems from the various interactions of neutron with carbon atoms, whereby α, β, γ or protons can be produced. The prevailing pulses are still those created by γ . Pulse shapes caused by neutrons are described in detail in [3, 4].

1.9.3 Scatter plots

An online pulse shape analysis has been run on all the aforementioned data sets. The parameters of the pulses are plotted in 2D histograms - in form of scatter plots. The aim is to find a way to distinguish between the various types of radiation in order to only select the spectrum of a single type of particles from a spectrum of a mixed source. The energy

spectrum is directly proportional to the measured area of the current pulses, therefore all the parameters are plotted as a function of the pulse area.

Every individual parameter can be attributed a set of qualifiers with which a certain part of the distribution can be rejected. There are two ways to apply the qualifiers. One is to set the minimum and maximum value for a specific parameter. The accepted pulses are those in between these two values. The minimum and the maximum qualifier are marked with a blue and a red line in the subsequent scatter plots. The second way is to apply a linear cut to the distribution in the scatter plot. The user can choose the slope of the line and to accept either the pulses above or below the line. The colour of the line is blue if the part above the line is accepted and red if opposite. Currently two scatter plots have this option implemented: area vs amplitude and area vs amplitude \times base width. The latter represents the Form Factor, which is discussed in section 1.6.2.

The sets of plots in figures 1.22, 1.20, 1.24 and 1.26 show the above listed parameters plotted as a function of the pulse area for ^{241}Am (electrons and holes), ^{90}Sr and ^{60}Co source, respectively. Any distinguishable difference between the plots of two sources would suggest that that particular parameter can be used to distinguish one type radiation from the other. For the most part the γ are considered the rejected pulses (greyscale colour palette) whereas α particles or neutrons are accepted (yellow colour palette). In special cases only a certain types of neutron interactions are accepted, as depicted in section 1.10.

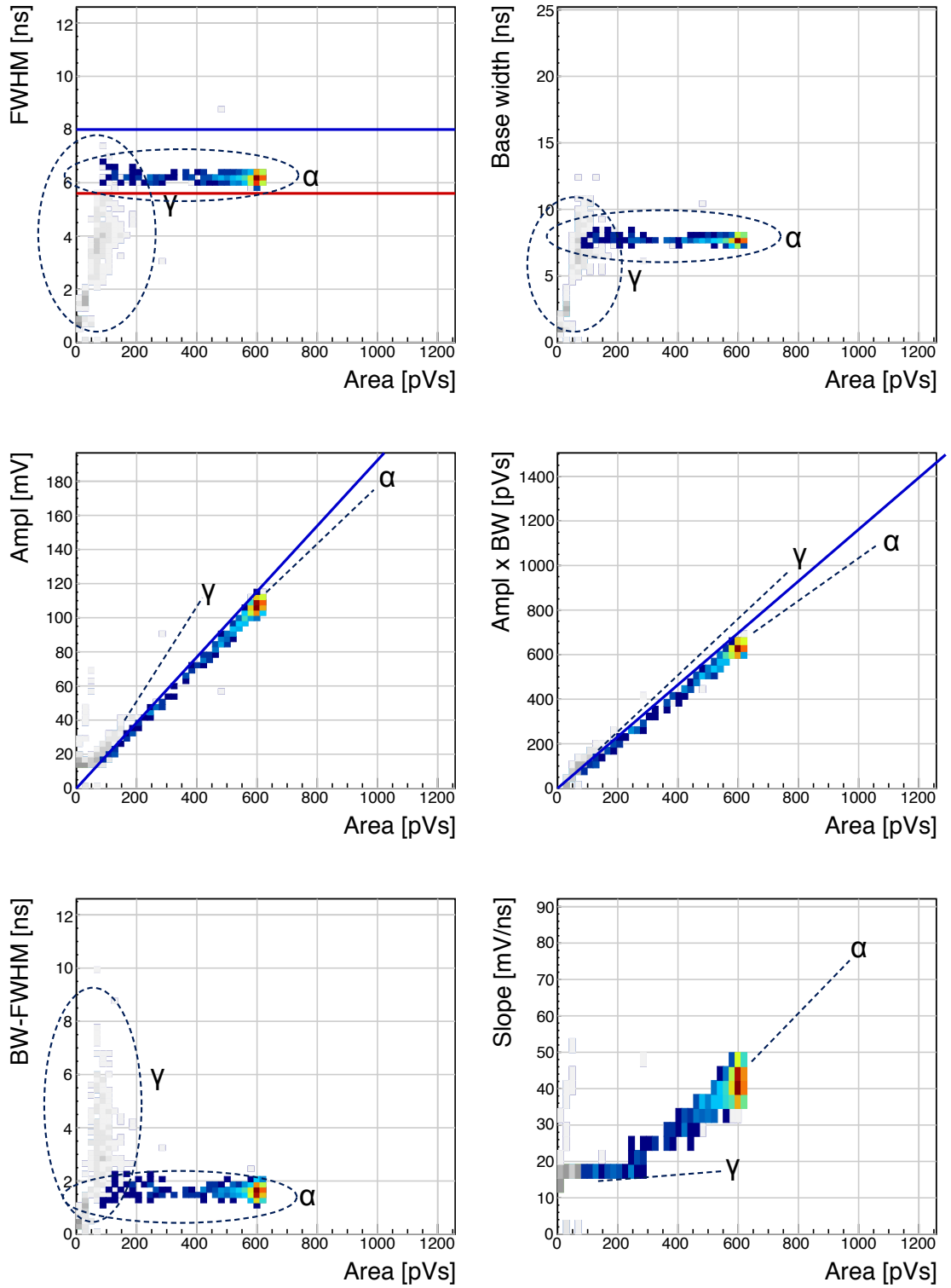


Figure 1.20: ^{241}Am , h^+ collection. Qualifier: FWHM.

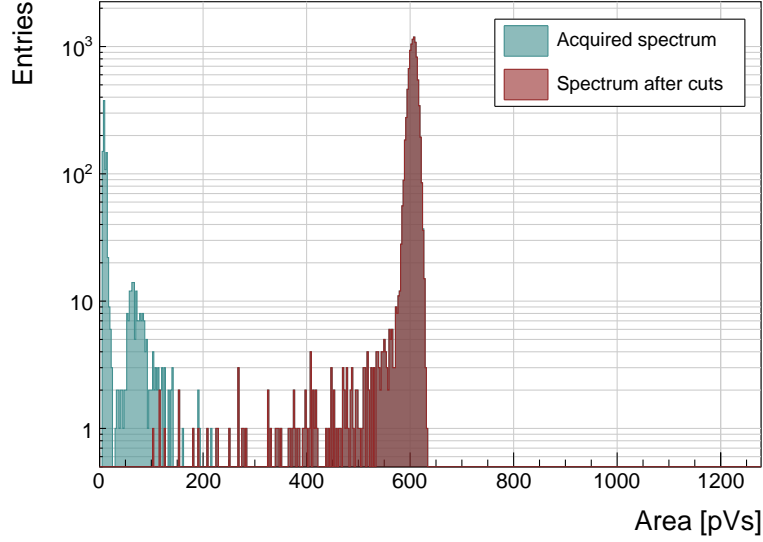


Figure 1.21: ^{241}Am area histograms for hole collection. The green histogram represents all collected data whereas the red one marks the data whereby the pulse parameters are within the qualifiers. The α peak at 600 pVs is clearly visible, followed by a γ quasi-Landau distribution with an MPV of ~ 70 pVs and a noise peak at the very left of the area distribution. These two contributions have been rejected by the qualifiers.

^{241}Am source, h^+ collection

The source emits α particles at ~ 5.5 MeV and 60 keV γ photons. Due to the losses in the air and in the electrode the measured α energy varies – between ~ 5 MeV down to 1 MeV. Figure 1.20 shows the parameter space of the acquired data for hole collection - Class 1. Width, amplitude and calculated area qualifiers have been used to identify the α pulses and reject the γ . Figure 1.21 shows a one-dimensional area distribution of the acquired data.

Width: A distinct horizontal line at 6.5 ns starting from 100 and peaking at 600 pVs shows the aforementioned spread of α energies. The width of the pulse remains constant. γ cluster overlaps with the α cluster at low energies. Width qualifier is used.

Base width: Wider than the FWHM, yet still constant over the entire range. High overlap with γ .

Amplitude: Linear increase with area. The coefficient for α pulses is lower than that for γ . Amplitude qualifier is used.

Calculated area: Barely distinguishable difference in slope coefficients for α and γ . Calculated area qualifier is used.

Base width – width: Minimal difference for α , high spread for γ as expected. At low γ area the overlap is high, so the qualifier cannot be used.

Slope: Linear increase with the area. Significant overlap in the low area range. A line of entries with a high slope at low area pertains to short noise pulses with a high spike.

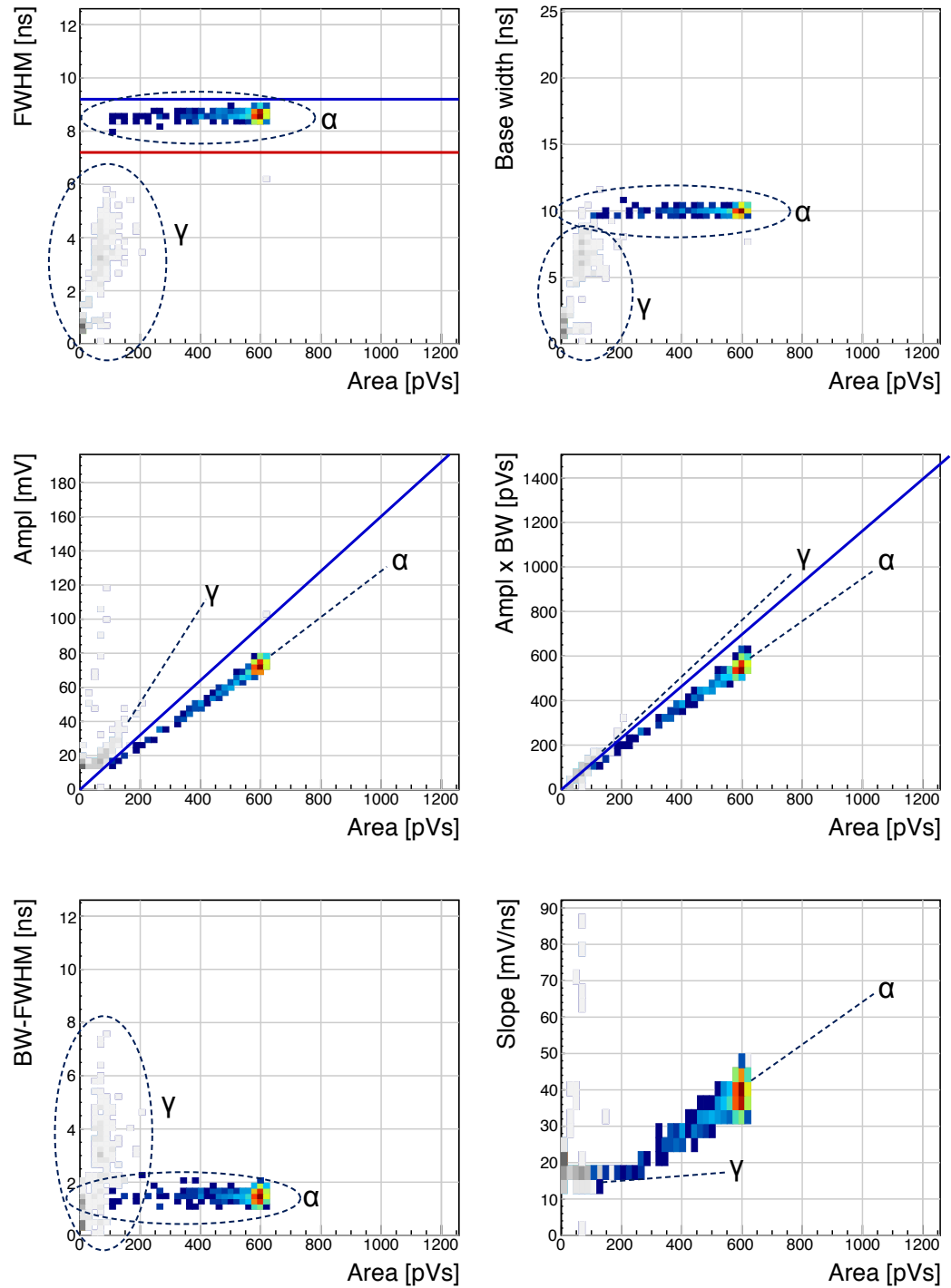


Figure 1.22: ^{241}Am , e^- collection. Qualifier: FWHM. Optional qualifiers: Amplitude, Form Factor.

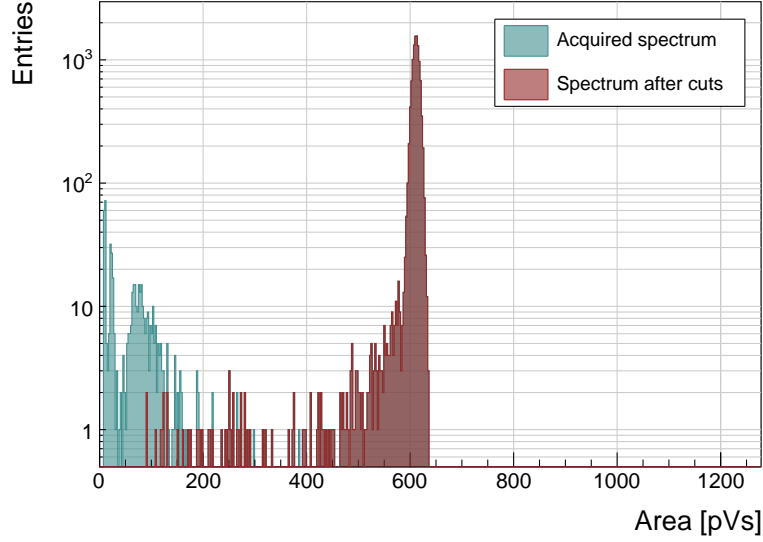


Figure 1.23: ^{241}Am area histograms for electron collection. The green histogram represents all collected data whereas the red one marks the data whereby the pulse parameters are within the qualifiers. The α peak at 600 pVs is clearly visible, followed by a γ quasi-Landau distribution with an MPV of ~ 70 pVs and a noise peak at the very left of the area distribution. These two contributions have been rejected by the qualifiers.

^{241}Am source, e^- collection

Figure 1.22 shows the parameter space of the acquired data for electron collection - Class 2. Width, amplitude and calculated area qualifiers have been used to identify the α pulses and reject the γ . Figure 1.23 shows a one-dimensional area distribution of the acquired data.

Width: A distinct horizontal line at 8.5 ns starting from 100 and peaking at 600 pVs shows the spread of α energies. The width of the pulse remains constant. γ cluster does not overlap with the α cluster at low energies as none of the γ pulses are as wide as the α . Width qualifier is used.

Base width: Wider than the FWHM, yet still constant over the entire range. Small overlap with γ .

Amplitude: Linear increase with area. The coefficient for α pulses is significantly lower than that for γ , also lower than that for hole collection. Amplitude qualifier is used.

Calculated area: Distinguishable difference in slope coefficients for α and γ . Calculated area qualifier is used.

Base width – width: Minimal difference for α , high spread for γ as expected. At low γ area the overlap is low, but due to low statistics.

Slope: Linear increase with the area. Overlap in the low area range. A line of entries with a high slope at low area pertains to short noise pulses with a high spike.

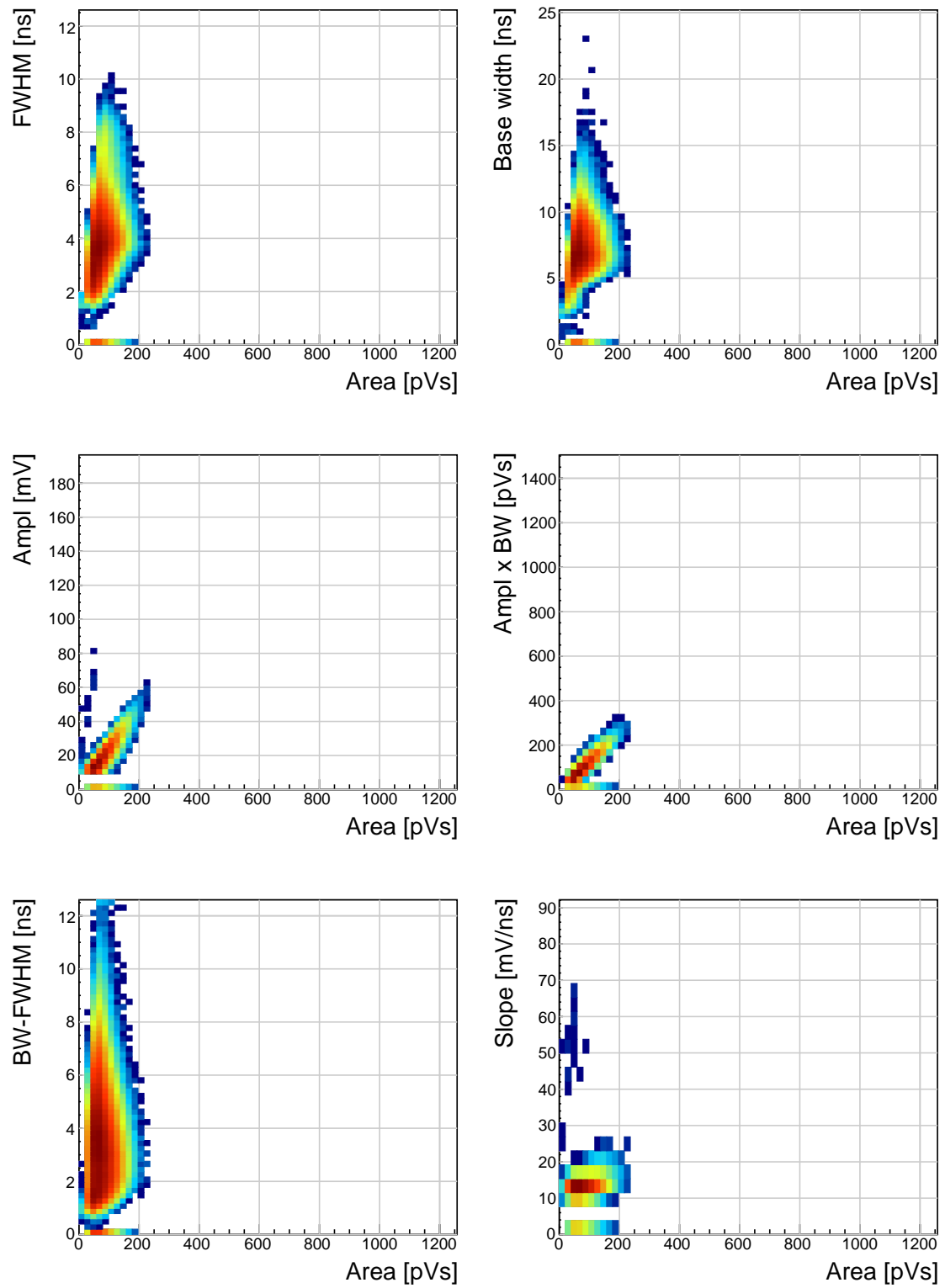


Figure 1.24: ^{90}Sr scatter plots.

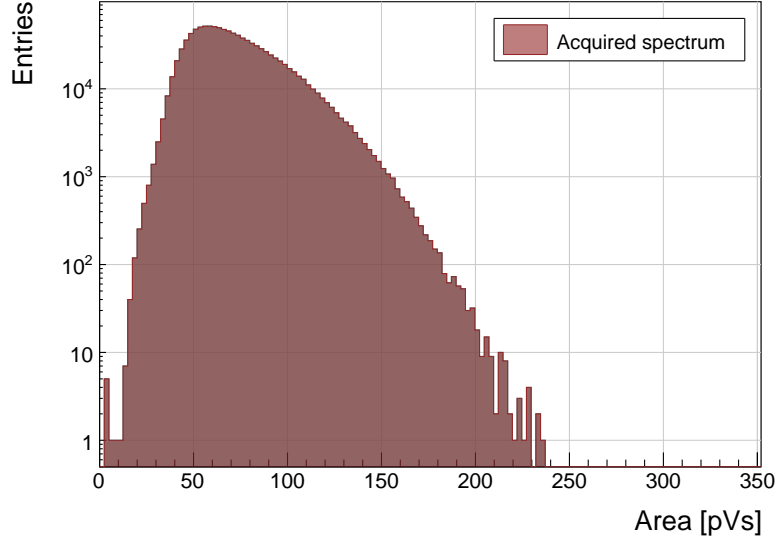


Figure 1.25: Area histogram for β particles. Relative to the 600 pVs α peak, the expected MPV of a β MIP is ~ 30 pVs, which is not the case in these distributions (peaking at 60 pVs). This is because the PSA device is a self-triggering system, which cuts the lower energetic particles with the trigger threshold. The resulting distribution is therefore only the top part of the real Landau distribution. This is a limitation of the device, governed by the analog noise of the current pre-amplifier.

^{90}Sr source

Figure 1.24 shows the parameter space of the acquired data for β particles - Class 3. Figure 1.25 shows a one-dimensional area distribution of the acquired data.

Width: The width of the β cluster is spread over a wide range and is not linearly dependent on the area. This implies that the pulse shapes are not necessarily triangular but have varying shapes.

Base width: Wider than the FWHM with a similar distribution.

Amplitude: Linear increase with the area. A line of entries with a high slope at low area pertains to short noise pulses with a high spike.

Calculated area: Linear increase with area.

Base width – width: A wide spread of entries.

Slope: A gentle linear increase with the area. A line of entries with a high slope at low area pertains to short noise pulses with a high spike.

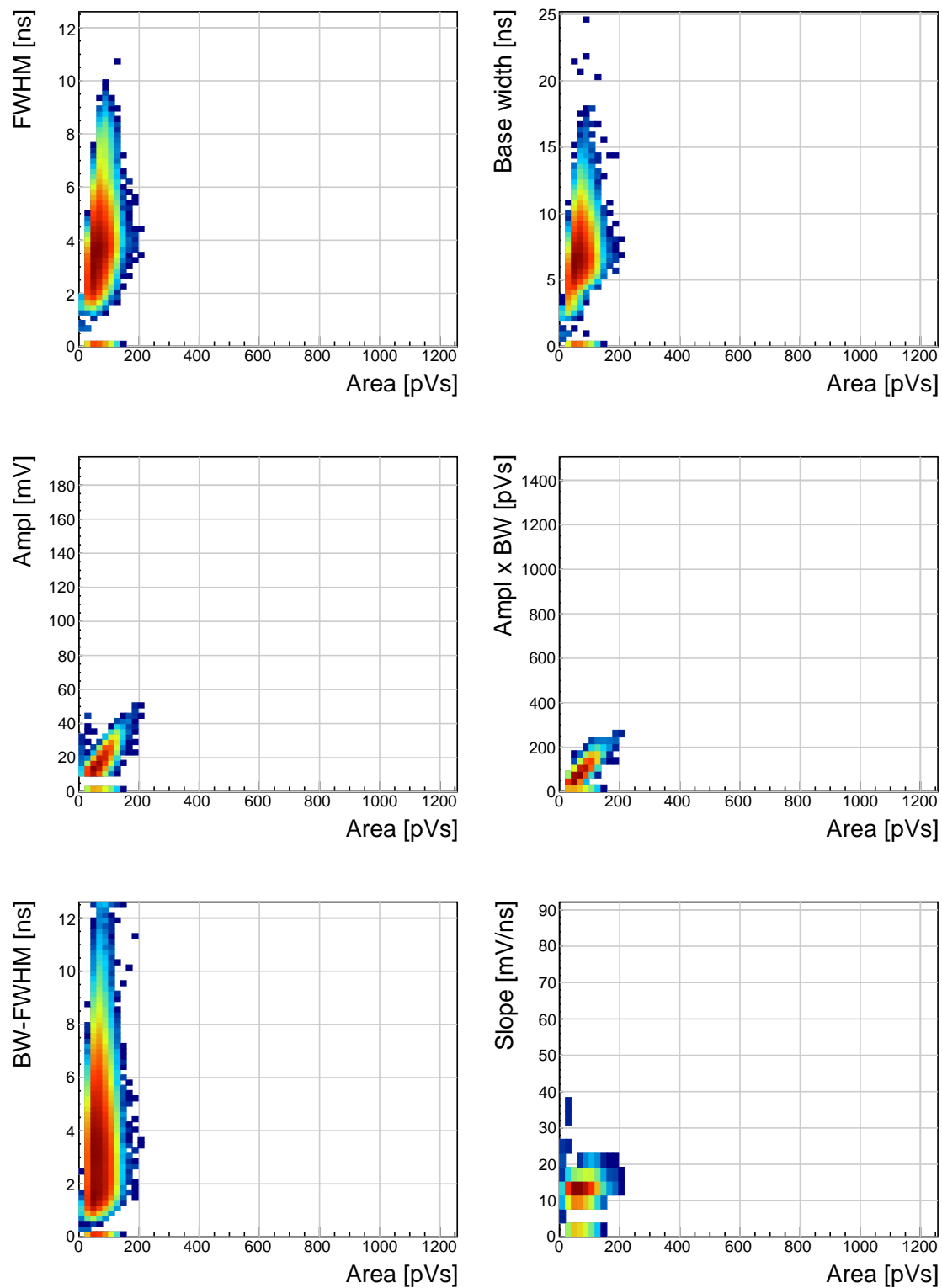


Figure 1.26: ^{60}Co scatter plots.

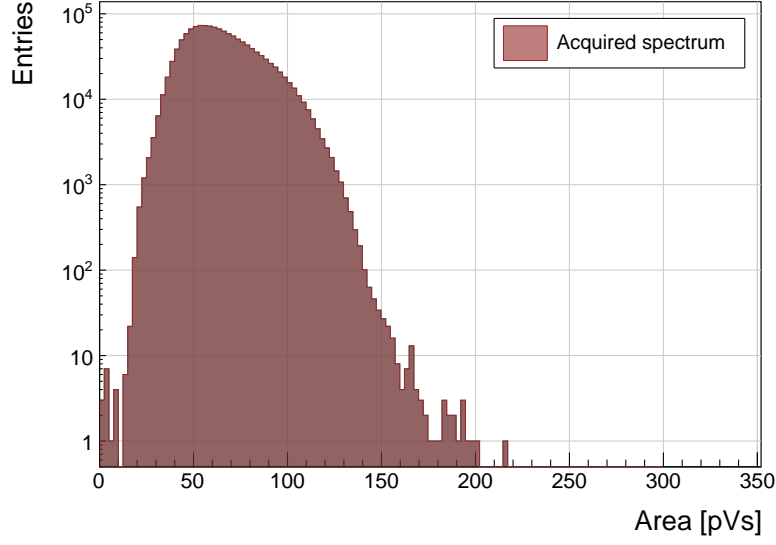


Figure 1.27: Area distribution of γ particles. Relative to the 600 pVs α peak, the expected MPV of a β MIP is ~ 30 pVs, which is not the case in these distributions (peaking at 60 pVs).

^{60}Co source

The parameter space of the ^{60}Co source overlaps entirely with that of the ^{90}Sr source. This renders it virtually impossible to distinguish between γ and β particles. Comparing the width of the γ and β and the high reach of the former, the electron collection of the alphas would need to be used to effectively discriminate between the two types of particles.

The one-dimensional histogram in figure 1.27 shows a quasi-Landau distribution with the MPV at ~ 60 pVs, which is in agreement with the background γ radiation emitted by the ^{241}Am source, as shown in figure 1.23 in the previous subsection. This is again not a pure Landau distribution – the real MPV should be peaking at 30 pVs, with a minimum expected area of 20 pVs at $2/3$ of the MPV. This is not possible to measure due to the high electronics noise of the amplifier and consequently a high trigger threshold to avoid noise triggers.

1.10 Applications in neutron instrumentation

The real-time pulse shape analysis procedure can be applied to more complex systems. This section includes three applications where the PSA has been applied.

Semiconductor-based neutron detectors provide a compact technology for neutron detection. However, the cross section of a neutron with diamond is very low, since it only interacts with the core of the atoms. Diamond is mainly used to detect charged particles.

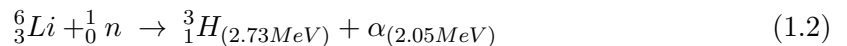
Research neutron reactors radiate a mix of particles, apart from neutrons also γ , which are considered a background radiation, which conceals the neutron spectrum. When measured with diamond, the signal from neutrons is difficult to distinguish from the photon spectrum. In addition, low energy neutrons do not cause nuclear reactions in the bulk. All in all, the neutron measurements in a reactor using a diamond sensor present a challenge. However, by means of the PSA, the neutron signal can be discriminated from the photon background to some extent. The following examples show how measurements of fast (n^+) and thermal (n^-) neutrons have been carried out by means of the PSA.

Note the changing scale on the x axis in the figures.

1.10.1 Thermal neutron flux monitoring

Research neutron reactors like TRIGA MARK II [?] at Atominstut [?] in Vienna are capable of emitting neutrons at a wide range of energies. The neutron flux is proportional to the current power of the reactor. It is therefore instrumental to monitor the neutron flux to make sure that the reactor operation is within the specified limits. However, the byproduct of the radioactive decays in the core is γ radiation, which has an energy range that overlaps with that of neutrons, making it difficult to measure the neutron flux. This is where PSA and diamond detectors come into play. This section describes the application of thermal neutron flux monitoring by means of the PSA.

Thermal neutrons do not interact with the diamond bulk due to their low kinetic energy (of the order of 0.012 eV). Hence a converter foil has to be added to produce second order effects. Incoming neutrons interact with the foil, producing a set of secondary particles. These can then be detected upon hitting the detector bulk. Common neutron interactions that are used in thermal neutron detection are $^{10}\text{B}(n,\alpha)^7\text{Li}$ reaction and $^6\text{Li}(n,\alpha)^3\text{H}$ reaction (α stands for ^4_2He , see equation 1.2). The focus in this section is on the latter. With a foil installed, there are several possibilities for neutrons to interact with the detector system. Each of these interactions ionises the diamond bulk in its own way, resulting in a specific shape of the current pulse. A neutron can: 1) interact with the foil, producing an α and a ^3H , 2) interact with a carbon atom in the lattice, producing an α and a γ or even three α . The thermal neutrons do not have enough kinetic energy to interact with the lattice, therefore the focus is on case (1). The equation for this reaction is the following:



The particles in the first case are produced outside the diamond and get stopped immediately upon hitting the sensor. The resulting pulses for both particles have a rectangular shape of the same width, because the carriers drift with the same speed in both cases. The difference is in the number of free carriers produced - the tritium creates more (proportional to the deposited energy), which in turn induces a higher pulse.

TRIGA MARK II neutron reactor emits large amounts of γ radiation in the energy range up to 3 MeV. This already affects the measurements of α particles, the energy of which peaks at 2.05 MeV in the case of ^6Li converter foil. However, γ background radiation can be suppressed by discriminating current pulses of γ from those induced by α particles. This idea has already been implemented in offline analysis in [1, 2]. The results show that the background γ can be subtracted successfully. In order to make sure that every single incident thermal neutron has been accounted for, the algorithm has been ported to FPGA where it detects and analyses particles in real time.

Measurements

ROSY readout device with the implemented Pulse Shape Analysis was put to a test at Atominstitut in Vienna. Their TRIGA neutron reactor is capable of delivering thermal neutrons with the energy 0.012 eV at a rate of $10^3 \text{ n cm}^{-2} \text{ s}^{-1}$, with a considerable γ background.

First, the device was calibrated using an unsealed monochromatic ^{241}Am source with the emitted particle energy $E_\alpha = 5.1 \text{ MeV}$ (taking into account the losses in the air). Then the diamond detector was exposed to the beam. Secondary reaction products (α and ^3H particles), created by neutrons hitting the converter foil, were detected by the diamond sensor, together with a significant photon background. Then the pulse identification algorithm was applied to discriminate between the reaction products and the γ .

The main parts of the detector are an sCVD diamond sensor sized $4.7 \text{ cm} \times 4.7 \text{ cm}$ and a $1.8 \text{ }\mu\text{m}$ thick ^6LiF converter foil, both embedded in an RF-tight PCB. The diamond sensor is biased with a bias voltage of $1 \text{ V}/\mu\text{m}$ and capacitively coupled to CIVIDEC's C2 40 dB wide bandwidth current preamplifier. A 5 m long BNC cable connects the preamplifier to CIVIDEC ROSY box. The detector assembly together with the preamplifier has to be placed in front of an exit hole of the reactor.

Note: this data set has been taken with an older version of the firmware, which only measured a limited number of pulse parameters.

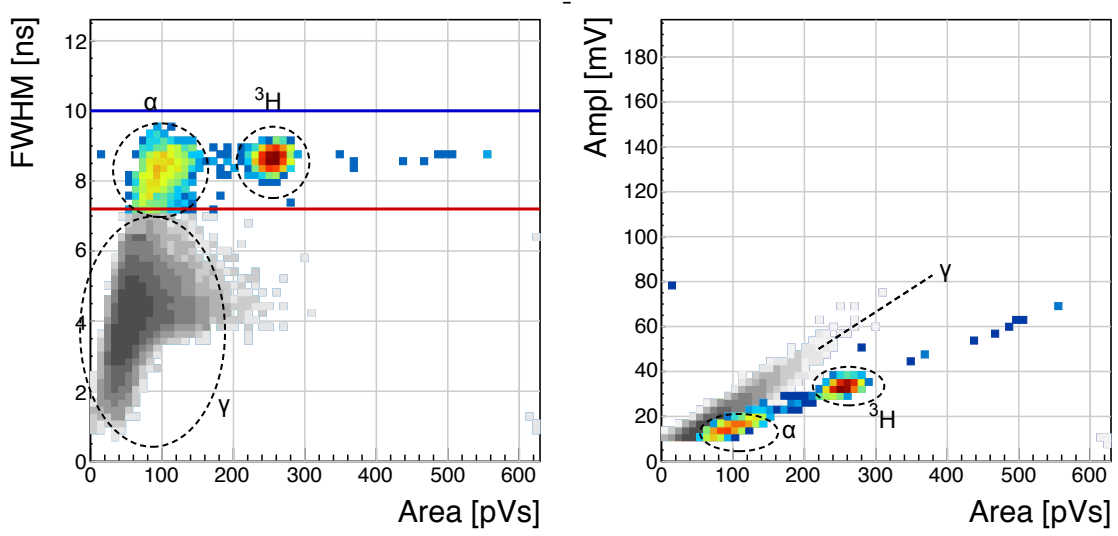


Figure 1.28: Thermal neutrons, γ . Qualifier: FWHM.

Results and discussion

The data shown in figure 1.28 show a high flux of γ , which covers a wide area range.

Width The ^3He peak is clearly visible in the top left plot and has almost no overlap with the γ cluster. The α cluster has a much lower energy and is in the same energy range as the γ . However, its width is higher and makes a separation between the γ and the α . By setting a qualifier to the right value, the photon background is cut away, leaving only the thermal neutron decay products in the data set.

Amplitude A clear difference between the linear coefficients is seen. However, at low area values the α peak is already hidden by the γ , which makes the amplitude qualifier insufficient.

The resulting one-dimensional area histogram before and after applied cuts is shown in figure 1.29. The blue distribution is the mixed field of background γ , tritium and α particles. The latter are completely hidden in the γ energy distribution. After applied qualifiers the α peak appears. There are 2422 and 1174 entries in the respective peaks, pointing to a $\sim 50\%$ detection efficiency of α particles. This loss is mostly due to energy losses in the air, which yields rectangular pulses with a low amplitude. The mean values are at 260 pVs and 100 pVs, which correspond to 2.1 MeV and 0.8 MeV. α therefore loses 60 % of its energy whereas tritium only loses 22 %.

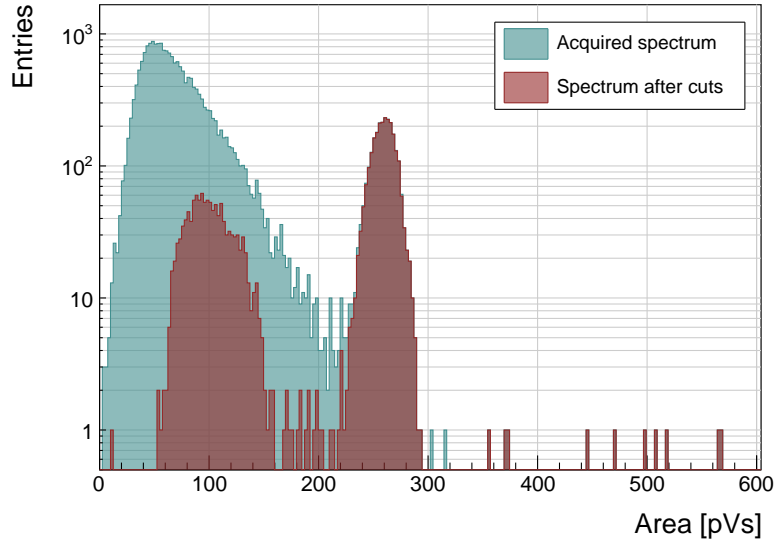


Figure 1.29: Energy spectrum after applied qualifiers reveals the tritium and the α peak.

To sum up, by applying the FWHM qualifier to the acquired data from the TRIGA neutron reactor, the α and tritium particles can be identified and separated from the γ background. The resulting cleaned data can be used to correctly count the thermal neutrons detected by the diamond sensor. The 50 % detection efficiency of α particles can be improved by minimising the distance between the ^6LiF foil and sensor, thus minimising the energy loss in the air.

1.10.2 Fusion power monitoring

Many research collaborations around the world are trying to develop a functional fusion reactor, which could provide a cleaner energy source. One of them is ITER [5], a research fusion reactor being built in France. The idea behind it is to harvest energy from the fusion of light atoms into a heavier one. For ITER the fuel chosen is a mixture of deuterium and tritium, which fuse into a helium atom at extremely high temperatures (plasma), emitting a highly energetic neutron as a byproduct. The equation is the following:



The α particle immediately deposits its energy within the plasma. The neutron, due to its neutral charge, continues its way out of the system where it is stopped. The stopping power is converted into energy, which heats the water into steam, which in turn spins the turbines, generating electricity.

It is possible to monitor the activity of the reactor by measuring the flux of neutrons emitted. Neutron diagnostics such as neutron cameras, neutron spectrometers and neutron flux monitors therefore provide robust measurements of fusion power. A high γ background makes it difficult to accurately measure the neutron flux. This is a motivation to use a diamond based detector with a real-time PSA algorithm.

The neutrons emitted are 14 MeV mono-energetic fast neutrons. The most accurate and efficient way to detect them with a diamond detector is by means of a $C_{12}(n,\alpha)$ reaction with a carbon atom in the ballistic centre [6]. In this region the positive and negative charge carriers created by α that start drifting in the opposite directions need the same time to reach the opposite electrodes.

Measurements

The ${}^{239}\text{Pu}$ Be neutron source has been used to simulate the fusion reactor. It emits a mixed field of neutrons and γ with a wide range of energies. The neutrons are rarely detected with diamond – the interactions happen mostly in the electrodes on either side of the detector. The α particles created by the interactions are detected by the diamond. Depending on the side of the interaction, the created pulse is either due to hole or electron collection. These two interactions make the two distinct lines in the *width* plot at 9 ns and 6 ns, as shown in figure 1.32, top left plot.

A very interesting interaction point is the ballistic centre [6, 4] of the diamond. A ballistic centre is the position from which it takes the holes and the electrons the same amount of time to drift to the respective electrodes. In this case the shortest possible pulse is created. Conversely, to conserve the collected charge and thus the pulse area, the pulse amplitude must be the highest at the ballistic centre. The entries in between are created by neutron interactions at random positions in the diamond, which produce pulses of various shapes.

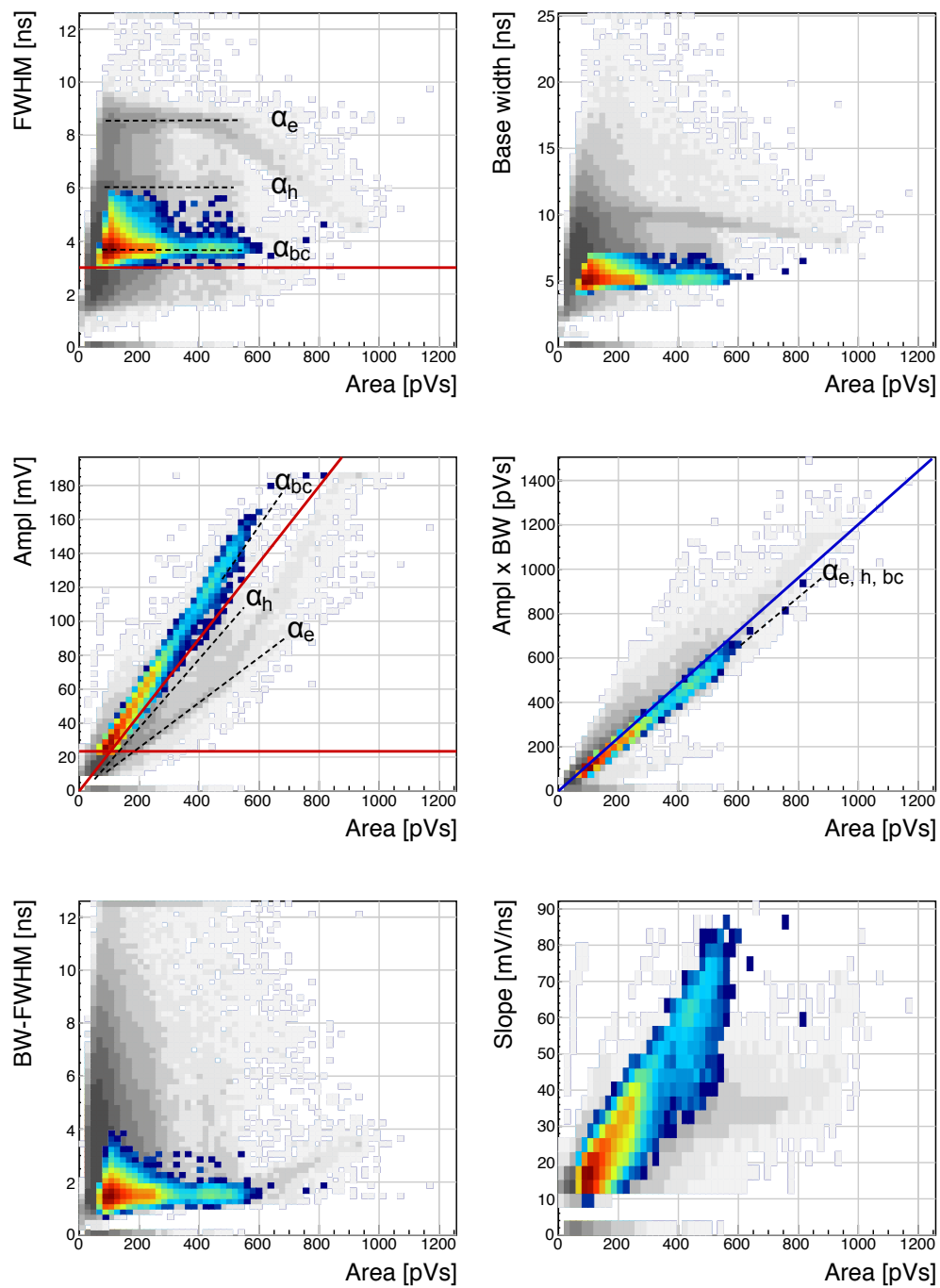


Figure 1.30: ^{239}Pu Be. Qualifiers: BW-FWHM, FWHM, Form Factor

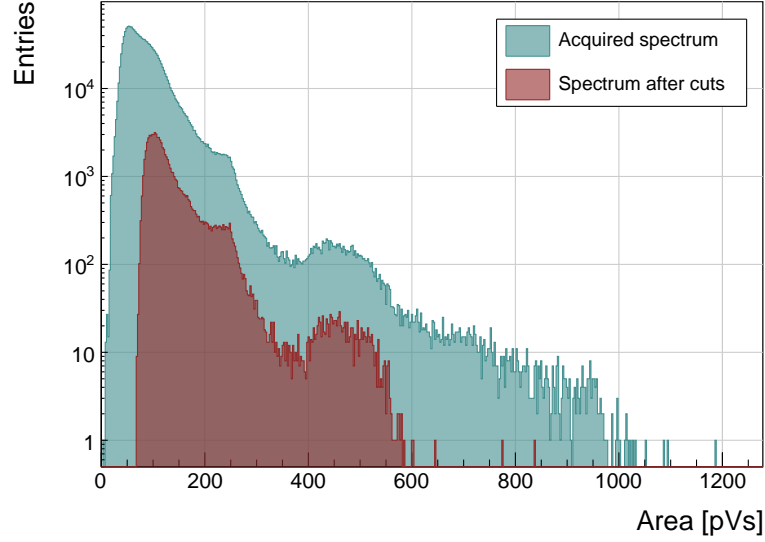


Figure 1.31: ^{239}Pu Be, energy distribution of the neutrons interacting in the ballistic centre.

Results and discussion

Coming back to the motivation, the most efficient way of counting the 14 MeV neutrons is through the measurement of the neutrons interacting in the ballistic centre [6, 4]. To extract this type of interaction several qualifiers must be used. The first possibility is the FWHM set to 3–5 ns. However, this time the cuts on the *width* and the *calculated area* are preferred. First, a minimum constant amplitude qualifier is set to 22 mV, as shown in figure 1.32, middle left plot. Then a linear amplitude qualifier is set such that only the pulses with the highest amplitude for every area value are taken. This ensures that the high pulses from the ballistic centre are chosen. Second, a maximum linear amplitude \times base value qualifier is set such that only the pulses bearing the closest resemblance to a rectangle are chosen, as shown in figure 1.32, middle right plot. In this space the entries at the bottom of the distribution are bearing more resemblance to a rectangle whereas those at the top are more akin to triangles.

The resulting *width* plot after applied qualifiers highlights the entries with a FWHM of 4 ns, which is the width of the pulses induced by neutrons interacting in the ballistic centre. This proves that these combined qualifiers indeed pinpoint these neutron interactions. The final one-dimensional area/energy distribution of the neutrons interacting in the ballistic centre is shown in figure 1.33.

The result could be further improved by further constraining the identification, e.g to define the minimum FWHM constant qualifier and the minimum slope constant qualifier. To sum up, by applying the appropriate qualifiers to the data, the neutron interactions in the ballistic centre can be identified.

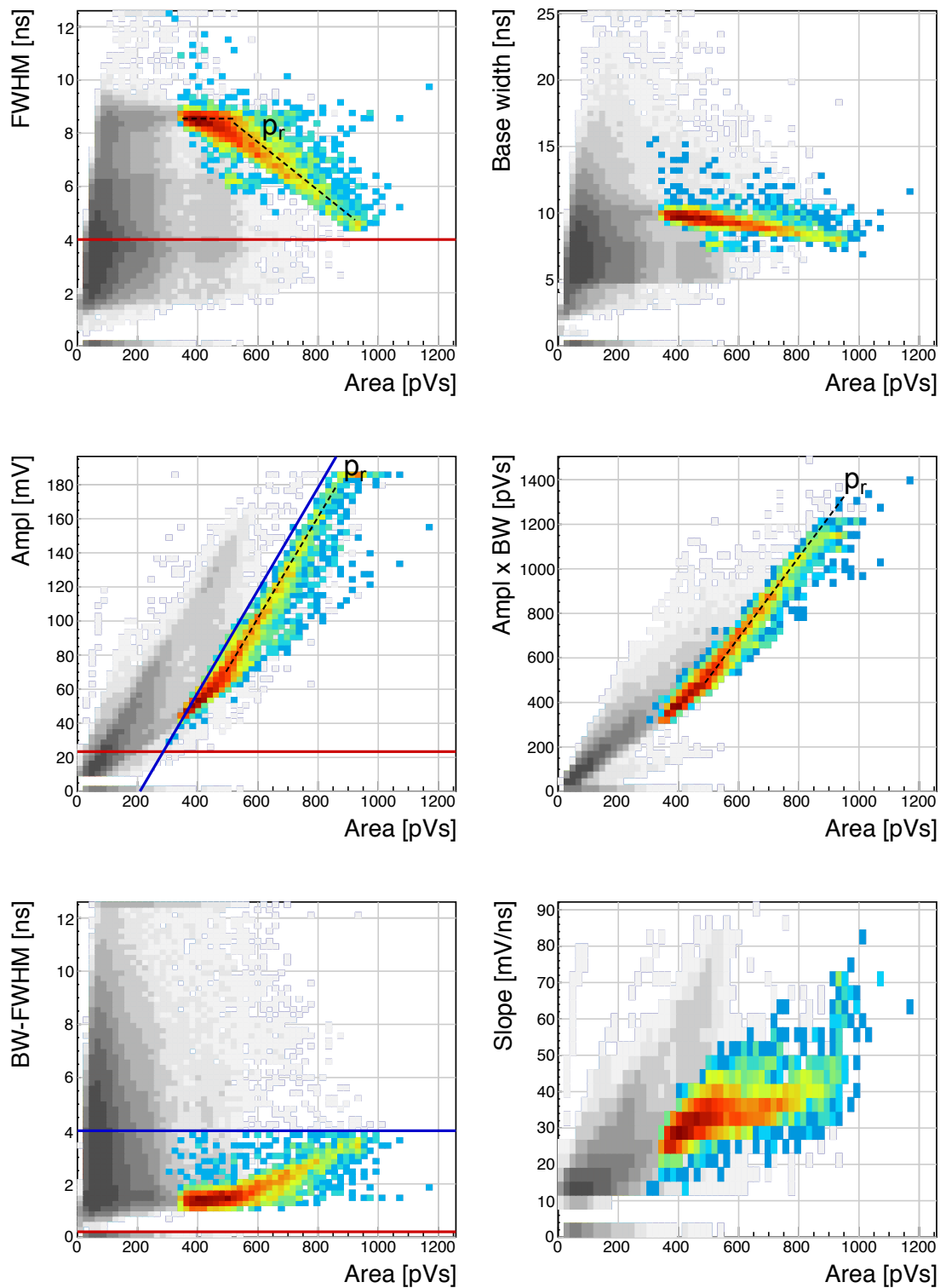


Figure 1.32: ^{239}Pu Be. Qualifiers: BW-FWHM, FWHM, amplitude, linear amplitude

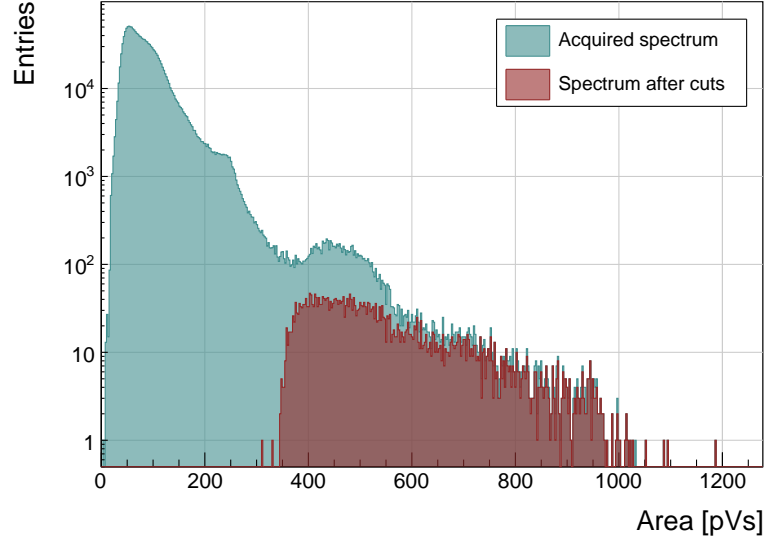


Figure 1.33: ^{239}Pu Be, energy distribution of the neutrons creating a recoil proton.

1.10.3 Recoil proton monitoring

High energy neutrons are typically detected indirectly through elastic scattering reactions. They collide with the nucleus of atoms in the detector, transferring energy to that nucleus and creating an ion, which is detected. If the hydrogen ion – a proton – is created, it travels through the sensor while ionising it and, depending on its initial energy, stops in the sensor or exits it with some residual energy. Its specific parametric signature is discussed in section 1.9.1.

Measurements

As in section 1.10.2, a ^{239}Pu Be has been used as a source of high energy neutrons.

Results and discussion

The most important qualifier for extracting the recoil protons is the amplitude. However, in this case the constant qualifiers do not help, nor does the linear qualifier starting at 0. To cut the recoil proton strand the starting point of the linear amplitude qualifier line has to start at a higher area value, 200 pVs in this case (shown in the *amplitude* plot in figure 1.32). Other qualifiers are set only to clean the outliers.

The measured parametric signature is not fully in agreement with that in figure 1.18. However, the steady fall in the *width* plot is clearly seen. The resulting one-dimensional plot after applied qualifiers is shown in figure 1.33.

To sum up, recoil protons can be extracted from a mix of created particles after neutron interactions with the diamond sensor.

1.10.4 Fast and thermal neutron monitoring

The CROCUS reactor at EPFL [7] is a research neutron reactor. The research group working on the reactor is interested in measuring neutrons with energies between 1–2 MeV, which is overlapping with the γ background energy range.

The highest output power of the CROCUS reactor is 100 W. Currently there are fission chambers that carry out the neutron counting, which is a measure of the activity of the reactor. The new goal is to measure both neutrons and γ , but separately. The pulse shape analysis is a good solution for this task. For this, a 400 μm thick diamond detector with a specially designed casing was added to measure the activity. The ^6LiF foil was added for conversion of thermal neutrons. The ROSY box with the integrated PSA routine was used for signal analysis.

Measurements

At the highest reactor activity the real-time system counts and analyses particles at a rate of $\sim 1.5 \times 10^5 \text{ s}^{-1}$. The results from a test run at 10 W output power are shown in figure 1.34. The data include a mixed field consisting of fast neutrons, γ and of α and ^3H particles as products of thermal neutron decay in the ^6LiF foil in front of the detector. The energy deposited in the diamond is not as high as that from the ^{239}Pu Be source. In addition, the analog noise during this measurement is higher than in the previous application. These conditions combined make particle identification at CROCUS a challenging task.

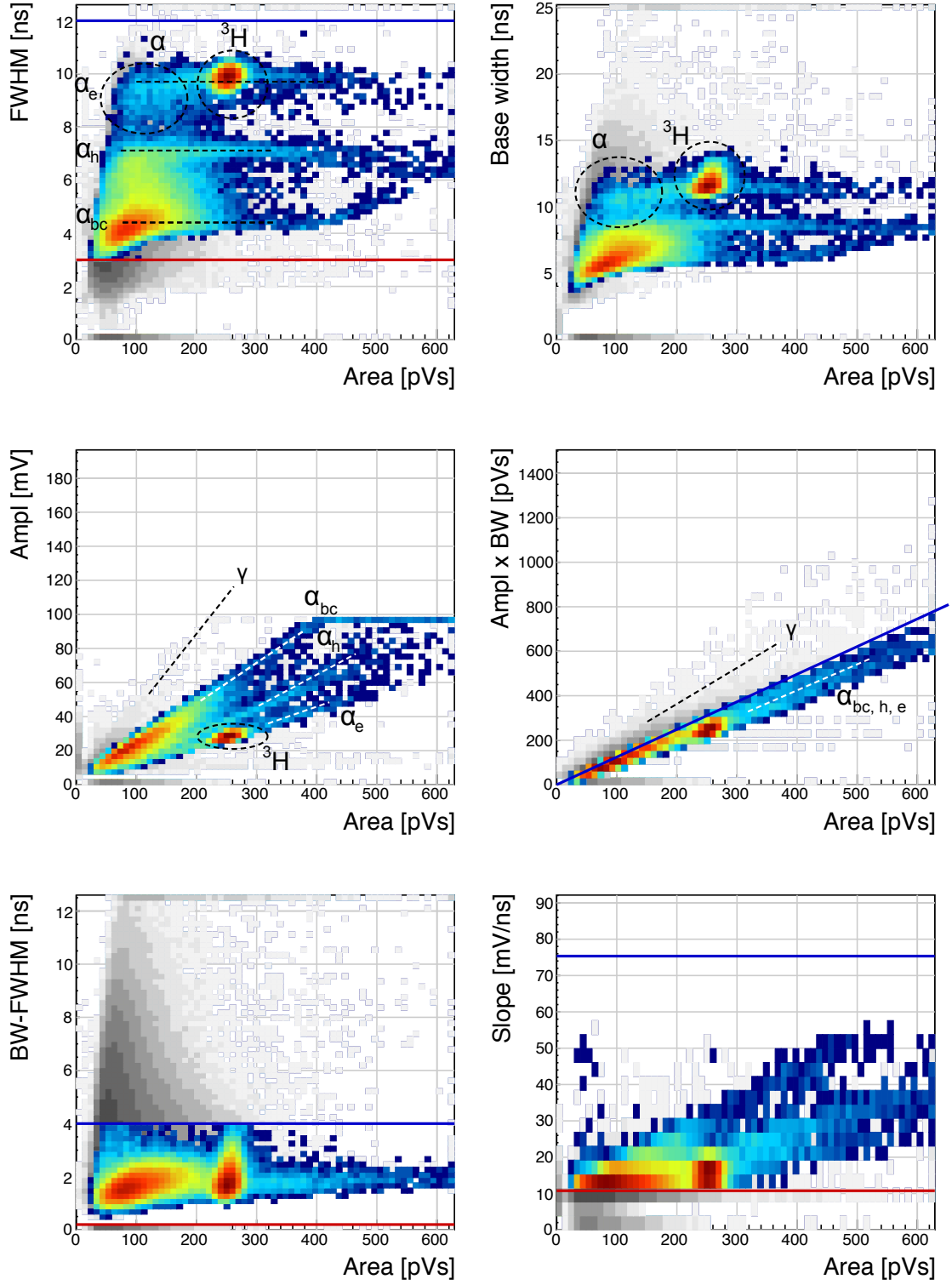


Figure 1.34: Fast neutrons, thermal neutrons, γ . Qualifiers: BW-FWHM, FWHM, Form factor, Slope.

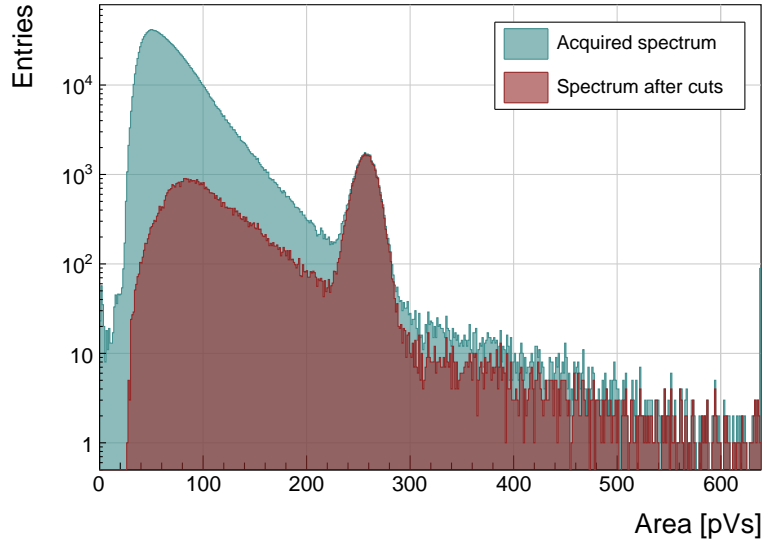


Figure 1.35: Energy spectrum in CROCUS before and after applied qualifiers.

Results and discussion

The aim of this exercise is to identify both thermal and fast neutrons. For this the main qualifier used is the Form Factor - the linear line in the *calculated area*. Additional FWHM, FWHM-BW and slope constant qualifiers are used to clean the outlying entries. The resulting accepted entries in figure 1.34 have the distinctive three-line fast neutron signature in the *width* plot with two superimposed islands by the α and ^3H cluster produced by thermal neutrons in the ^6LiF foil. The γ background is sufficiently suppressed. The resulting one-dimensional histogram of the area/energy distribution is shown in figure 1.35.

To sum up, by applying the Form Factor qualifier both fast and thermal neutrons can be identified, suppressing the γ background.

1.11 Conclusion

This chapter describes a system that can identify the type of radiation in real time. The system is implemented on an FPGA in a CIVIDEC ROSY box and is used with diamond detectors. The signal from the diamond sensor is read in and analysed in the firmware. First the shape of the pulse is parametrised. Then the logic determines the type of particle according to the user defined cuts. Finally the parameters are written into a histogram, which is read out by the user. The firmware is designed to carry out the pulse shape analysis of a single pulse in ~ 200 ns, yielding a maximum pulse rate of 6×10^6 particles per second. The rate as well as the linearity the measurement stability with respect to noise have been verified using a pulse generator. Then several radioactive sources were used to calibrate the device. Finally the system has been set up in two neutron reactors to test the operation in a mixed field containing thermal neutrons, fast neutrons and γ . The identification can be optimised using a combination of qualifiers to achieve the desired effect.

Bibliography

- [1] P. Kavargin, P. Finocchiario, E. Griesmayer, E. Jericha, A. Pappalardo, and C. Weiss. *Pulse-shape analysis for gamma background rejection in thermal neutron radiation using CVD diamond detectors. Nuclear Instruments and Methods in Physics Research A*, (795), 2015.
- [2] E. Griesmayer, R. Bergmann, H. Böck, M. Cagnazzo, P. Kavargin, B. Morgenbesser, and M. Villa. *A Novel Neutron Flux Monitor Based On Diamond Detectors at the Vienna TRIGA Mark II Reactor. submitted to the proceedings of ICRR 2015*, 2015.
- [3] C. Weiss, H. Fraiss-Kölbl, E. Griesmayer, and P. Kavargin. *Ionization signals of diamond detectors in fast neutron fields. publication in preparation*, 2016.
- [4] C. Weiss. A CVD diamond detector for (n,α) cross-section measurements. PhD thesis, TU Wien, Vienna, 2014.
- [5] *ITER fusion reactor*. <https://www.iter.org/>.
- [6] P. Kavargin, E. Griesmayer, F. Belloni, A.J.M. Plompen, P. Schillebeeckx, and C. Weiss. $^{13}\text{C}(n,\alpha_0)^{10}\text{Be}$ cross section measurement with sCVD diamond detector. *submitted to EPJA*, 2016.
- [7] *CROCUS neutron reactor*. <http://lrs.epfl.ch/page-55655-en.html>.